

# Mechanism-based modeling of solute strengthening: application to thermal creep in Zr alloy

Wei Wen, Laurent Capolungo, Carlos N. Tomé

Materials Science and Technology Division, Los Alamos National Laboratory  
Los Alamos, NM 87545

## Abstract

In this work, a crystallographic thermal creep model is proposed for Zr alloys that accounts for the hardening contribution of solutes via their time-dependent pinning effect on dislocations. The core-diffusion model proposed by Soare and Curtin (2008a) is coupled with a recently proposed constitutive modeling framework (Wang et al., 2017, 2016) accounting for the heterogeneous distribution of internal stresses within grains. The Coble creep mechanism is also included. This model is, in turn, embedded in the effective medium crystallographic VPSC framework and used to predict creep strain evolution of polycrystals under different temperature and stress conditions. The simulation results reproduce the experimental creep data for Zircaloy-4 and the transition between the low ( $n \sim 1$ ), intermediate ( $n \sim 4$ ) and high ( $n \sim 9$ ) power law creep regimes. This is achieved through the dependence on local aging time of the solute-dislocation binding energy. The anomalies in strain rate sensitivity (SRS) are discussed in terms of core-diffusion effects on dislocation junction strength.

The mechanism-based model captures the primary and secondary creep regimes results reported by Kombaiah and Murty (2015a, 2015b) for a comprehensive set of testing conditions covering the 500 to 600°C interval, stresses spanning 14 to 156 MPa, and steady state creep rates varying between  $1.5 \cdot 10^{-9} \text{s}^{-1}$  to  $2 \cdot 10^{-3} \text{s}^{-1}$ . There are two major advantages to this model with respect to more empirical ones used as constitutive laws for describing thermal creep of cladding: 1) specific dependences on the nature of solutes and their concentrations are explicitly accounted for; 2) accident conditions in reactors, such as RIA and LOCA, usually take place in short times, and deformation takes place in the primary, not the steady-state creep stage. As a consequence, a model that accounts for the evolution with time of microstructure is more reliable for this kind of simulation.

## 1 Introduction

Zirconium alloys have been used as nuclear core materials in light water reactors (LWRs) over the past 50 years. These alloys show low thermal neutron absorption rate, excellent creep strength under high-temperature environments, and superior corrosion resistance, which have effectively prolonged the service life and enhanced the accident tolerance of the reactors. During in-reactor operation, the material is exposed to temperature, pressure and irradiation conditions, which leads to dimensional changes induced by irradiation creep, irradiation growth, and thermal

creep. While thermal creep effects are regarded as minor during normal in-reactor operation conditions, they become relevant under abnormal or accident conditions leading to abrupt temperature increases. Therefore it is essential to understand the thermal creep mechanisms in Zr alloy and their relationship to the mechanical properties.

The experimental studies of the creep behavior of Zr alloy can be traced back to the work of Rosinger et al. (1979) and Garde et al. (1978), who performed tensile creep tests on Zircaloy-2 and Zircaloy-4. Recently, Kombaiah and Murty (2015a, 2015b) conducted tests on Zircaloy-4 within the temperature range of 500°C-600°C, and the results provide a valuable database to understand mechanisms during thermal creep. Fig. 1 summarizes the steady-state creep rates reported in Kombaiah and Murty. It shows that the creep rates vary by more than six orders of magnitude within the temperature and stress intervals involved. According to Kombaiah and Murty, results can be classified into three regimes. At low stress (<40MPa), the reported creep rates show a linear dependence on the creep stresses, which implies the creep behavior in this regime is mainly controlled by diffusional creep mechanisms, such as the Nabarro-Herring creep and Coble creep. At higher stresses creep is consistent with a power law relationship, but with two sub-regimes of power  $n \approx 4$  at moderate stress and  $n \approx 9$  at high stress. Notice that similar behavior (transition between moderate and high stress regimes with different power  $n$ ) has also been observed in earlier works of Zr-Nb alloys (Charit and Murty, 2008; Murty et al., 2005; Pahutová et al., 1976). Although the values of  $n$  vary with the chemical composition of the materials, the transition between the two regimes always occurs in the creep rate interval of  $10^{-7} : 10^{-6} s^{-1}$ . In addition, anomalous strain rate sensitivity (SRS) has also been observed in Zr alloy. Graff (2006) performed tensile tests on Zr702 and Zr-Hf and determined their SRSs at different temperatures. The results show a dip of SRS at around 400°C. Such low or even negative SRSs is usually associated with the dynamic strain aging (DSA) induced by the diffusion of solute atoms to dislocations.

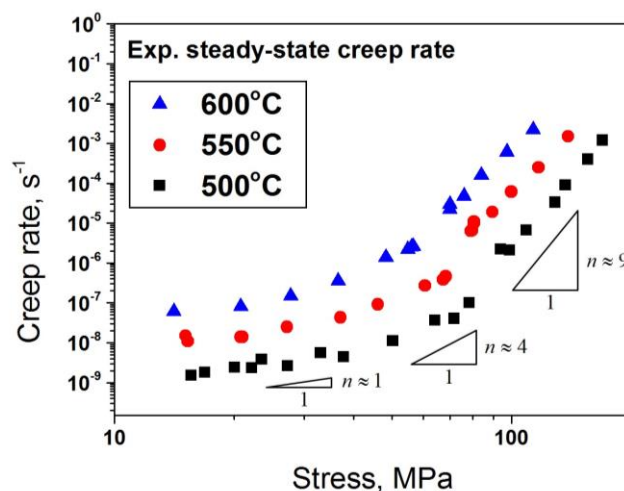


Fig. 1. Experimental steady-state creep rate reported in Kombaiah and Murty (2015a, 2015b).

To interpret and predict the experimental evidence in Zr alloys mentioned above, it is necessary to understand the mechanisms activated during the creep tests. In the 1960s Barrett and Nix (1965) proposed a steady-state theory assuming that the glide of the jogged screw dislocations is limited by the motion of jogs. During deformation, screw dislocations in prismatic planes tend to cross-slip and form jogs on the basal planes. These jogs are edge in character and can move conservatively on the basal planes and non-conservatively (climb) in the perpendicular direction. The motion of these jogged screw dislocation is affected by many factors. Depending on the stress and the jog status, they may be either pinned at the jogs, or bow-out and continue to glide. In the theory of Barrett and Nix (1965), the creep rate is governed by the climb of the jogs, which is diffusion controlled and driven by the line tension of the dislocation pinned between the jogs. Later, based on the same assumption, Viswanathan et al. (2002, 1999) adapted the formulation of Hirth and Lothe (1983) to account for the actual processes associated with the jog height and spacing. Morrow et al. (2013) utilized this modified jogged-screw model to predict the creep behavior of Zircaloy-4 for temperature between 260°C and 427°C. However, the application of this model may be limited to a certain temperature range since the formation of jogs is temperature dependent. For the microstructure characterization at a higher temperature (500°C-600°C) (Kombaiah and Murty, 2015a, 2015b), the jog density was reported to be very low, implying the creep behavior is dominated by some other mechanisms. The disappearance of the jogs at high temperature has also been reported elsewhere (Ecob and Donaldson, 1985). Moreover, the jogged-screw theory is challenged by a recent in-situ TEM study (Caillard et al., 2015) done at similar temperature (250°C-450°C) as Morrow et al. (2013), where the climb of jogs is not observed.

While the jog density is very low at higher temperatures, fully formed subgrain boundaries have been detected by Kombaiah and Murty (2015a, 2015b), consisting of pure edge dislocations and the special ‘honeycomb’ wall structure. The ‘honeycomb’ boundary, also recognized as Frank network (Hayes et al., 2002; Poirier, 1976), is reported in Kombaiah and Murty (2015a) as a 2-D structure on the basal plane. According to Kombaiah and Murty (2015a, 2015b), its formation starts with the interaction between the screw dislocations on different prismatic planes, followed by cross-slip. The incoming dislocations will repeat this process. As a result, the ‘honeycomb’ network is formed. In addition to this basal plane boundary, another ‘honeycomb’ structure located on the plane perpendicular to the  $\langle 11\bar{2}3 \rangle$  direction is reported by Kombaiah and Murty (2015a, 2015b). Kombaiah and Murty indicated that this type of boundary is composed of dislocations lying on the intersection of the prismatic plane and the wall plane. These dislocations are of a mixed type, and they may move on the wall plane through the climb process, which is necessary for the network formation. The ‘honeycomb’ boundaries are intensively formed at elevated temperatures due to the high activity of both climb and cross-slip. Notice that they are also detected at lower temperatures but in an incomplete form (Moon et al., 2006; Morrow et al., 2013).

Solute dragging may also affect the creep response in Zr alloys. When a dislocation is traveling freely within the matrix, it will interact with the solutes around it and experience a dragging stress. This dragging stress is a function of solute atoms bulk diffusivity and depends linearly on the dislocation speed. According to Caillard et al. (2015), the velocity of free traveling dislocations is of order 10nm/s, while the dragging resistance is under 50MPa. However, it has been reported that high stresses will build up at a dislocation pinned for a long period at obstacles. When unpinned, it will achieve immediately a very high velocity until it reaches the next obstacle (Castany et al., 2007).

Soare and Curtin (2008a, 2008b) developed a hardening law considering the effects of the diffusion of solutes in the dislocation core. This model is based on a series of atomistic and mesoscale simulations (Curtin et al., 2006; Olmsted et al., 2006; Picu, 2004) aiming to study the Dynamic Strain Ageing (DSA) phenomenon. The core-diffusion theory suggests that when a clustered dislocation is immobilized, the surrounding impurities tend to diffuse within the dislocation core area and thus introduce an extra energy binding the dislocation to its current position. Therefore an extra stress is required for unpinning to take place. Moreover, the core-diffusion will also increase the effective dislocation-dislocation junction strength, which is suggested to be responsible for the anomalous SRS. Although the core-diffusion model, as well as the foundational atomic level simulations, focuses on the behavior of Al-Mg alloy, we believe the theory is applicable to Zr alloy due to the presence of solutes in both materials.

In the present work, a physics-based thermal creep constitutive model is proposed based on the core-diffusion theory and is employed to predict the behavior of Zircaloy-4 under creep tests at various temperatures and stresses. In this model, the hardening equations of Soare and Curtin (2008a, 2008b) are coupled with a recently proposed framework accounting for the heterogeneous distribution of internal stresses within grains (Wang et al., 2016, 2017). This model, which is embedded in the crystallographic visco-plastic self-consistent (VPSC) framework (Lebensohn et al., 2007; Lebensohn and Tomé, 1993), will be introduced in section 2. In section 3, the predicted thermal creep behavior is presented and compared with the experimental data given in Kombaiah and Murty (2015a, 2015b) for Zircaloy-4 under various temperatures and applied stresses. With the addition of Coble creep mechanism, this model is capable of reproducing the transition between the low, intermediate and high power  $n$  regimes. The role of core-diffusion of solutes on strain rate sensitivity is also discussed.

## **2 Thermal creep model**

The constitutive model developed in this work aims to describe the thermal creep behavior of Zr alloy with randomly distributed solute atoms (Oxygen, Tin, etc.), and quantify the effects of each solute diffusion related mechanism occurring

simultaneously during the deformation. An extensive experimental characterization of the role of Oxygen upon thermal creep of Zircaloy-4 can be found in the work of Warda et al. (1973). In our model the creep strain is assumed to be accumulated through dislocation motion and Coble creep. These two mechanisms take place simultaneously during the plastic deformation. Therefore, the total strain rate in each grain is written as:

$$\dot{\boldsymbol{\varepsilon}}^p = \dot{\boldsymbol{\varepsilon}}^d + \dot{\boldsymbol{\varepsilon}}^{coble} \quad (1)$$

## 2.1 Dislocation driven creep

In the present work, the dislocation motion refers to conservative gliding on the slip planes. The exclusion of the climb mechanism will be discussed in the following sections. In this case, the dislocation motion induced strain rate  $\dot{\boldsymbol{\varepsilon}}^d$  can be written as the sum of the mean shear rates on all active slip systems:

$$\dot{\boldsymbol{\varepsilon}}_{ij}^d = \sum_s m_{ij}^s \bar{\dot{\gamma}}^s \quad (2)$$

where  $m^s = \frac{1}{2}(\mathbf{n}^s \otimes \mathbf{b}^s)$  refers to the symmetric part of the Schmid tensor.  $\mathbf{n}^s$  and  $\mathbf{b}^s$  are the normal and Burgers vectors of slip system  $s$ .

It is well-known that the stress distribution within a grain or subgrain is heterogeneous. As a consequence, some dislocations may be able to glide due to the high local stress state, whereas others may be immobilized if the local stress is insufficient to overcome the resistance. However, effective medium polycrystal models, such as the VPSC model employed in this study, assume that the stress and strain rate inside each grain are homogeneous. Therefore, it is necessary to express the mean mechanical response of the grain as an average over all sub-material points. Moreover, since the shear rate versus stress response in crystals is usually non-linear, such a treatment will also grant a better connection between the local atomistic-level simulations and the macroscopic performance.

In this work, the proposed model uses as a framework the theory originally proposed by Wang et al. (2016, 2017) in which each material point (grain) is regarded as decomposed into an infinite number of sub-material points, each having its own stress state depending on the local microstructure. In Wang et al. (2016, 2017), the mean shear rate  $\bar{\dot{\gamma}}^s$  in one material point (representing one grain) can be obtained as the integral of the local shear rates over all sub-material points. For dislocation glide, the mean shear rate of slip system  $s$  is expressed as:

$$\bar{\dot{\gamma}}^s = \int_{-\infty}^{\infty} \dot{\gamma}^s(\tau^s) P(\tau^s - \bar{\tau}^s) d\tau^s \quad (3)$$

where  $\dot{\gamma}^s$  represents the shear rate in one sub-material point with local resolved shear stress  $\tau^s$ .  $\bar{\tau}^s = \boldsymbol{\sigma} : \mathbf{m}^s$  denotes the mean resolved shear stress in one grain,  $\boldsymbol{\sigma}$

is the deviatoric stress tensor. The probability distribution function  $P(\tau^s - \bar{\tau}^s)$  in Eq. 3 represents the volume fraction of sub-material points with  $\tau^s$ . The analysis of the internal stress fluctuation induced by dislocation arrangements can be traced back to the theory of Wilkens (1970) which predicts symmetric line broadening with a Gaussian center part and non-Gaussian tails in the line profile. In the case of restricted randomly dislocation distribution within a diffracting domain, the entire line profile can be accurately described with a Gaussian distribution. Later, the theory proposed by Groma and Bakó (1998) indicates that the tail of the probability distribution of the internal stress decays with the inverse third power of the stress. This theory has been discussed and verified by Groma and Székely (2000), Wilkinson et al. (2014) and Kalácska et al. (2017). In the constitutive modeling framework of Wang et al. (2016, 2017), the internal stress distribution is assumed to be Gaussian. The rationality of this simplification can be justified as follows: the main purpose of incorporating the internal stress distribution in constitutive models is to connect the localized strain-stress response with bulk performance. In this case, one should only account for the stress fluctuations above the scale of the dislocation spacing and junction width, where the dislocation induced shear rate and the flow stress can be meaningfully defined. At this length scale, the averaged stress distribution, resulting from the superposition of stress fields of many dislocations, corresponds to the Gaussian central part in the theories of Wilkens and Groma. In addition, the power law tail induced by the high-stress regions near single dislocation cores should disappear. Therefore, following Wang et al. (2016, 2017), the internal stress distribution in the present work is given as a Gaussian function depending on the deviation of  $\tau^s$  from  $\bar{\tau}^s$ :

$$P(\tau^s - \bar{\tau}^s) = \frac{1}{\sqrt{2\pi}V} \exp\left(-\frac{(\tau^s - \bar{\tau}^s)^2}{2V^2}\right) \quad (4)$$

where  $V$  is the distribution variance, which is different for each material point. As discussed in Wang et al. (2016), the intragranular stress dispersion (responsible for peak broadening) may be assumed to be a function of the total dislocation density in the grain, and  $V$  is expressed as:

$$V = \eta\sqrt{\rho} \quad (5)$$

where  $\rho$  is the total dislocation density in one grain and  $\eta \approx 10^{-7}$  MPa/m is a scaling coefficient (Wang et al., 2016).

In the present model, the local shear rate on system  $s$  can be determined through the well-known Orowan's equation:

$$\dot{\gamma}^s = \rho^s b^s v^s \cdot \text{sign}(\tau^s) \quad (6)$$

where  $b^s$  is the magnitude of the Burgers vector, and  $v^s$  is the mean dislocation velocity. The latter is given by the mean spacing between obstacles (dislocation mean

free path  $\lambda^s$ ) and the total time a dislocation spends in this process, which includes the time traveling within the free spacing  $t_t^s$  and the waiting time at obstacles before the bypass  $t_w^s$ :

$$v^s = \frac{\lambda^s}{t_w^s + t_t^s} \quad (7)$$

In the present work, only the dislocations are considered as obstacles. The effective obstacle interspacing hinges on the nature of the barrier. For dislocation-type obstacle, it is associated with dislocation-dislocation interactions between slip systems. Thus, in this work, the law proposed by Franciosi and Zaoui (1982), and for which discrete dislocation dynamics simulations of Bertin et al. (2014) have demonstrated the statistical representativeness is used to express the dislocation mean free path in Eq. 8 as:

$$\frac{1}{\lambda^s} = \sqrt{\sum_s \bar{\alpha}^{ss'} \rho^{s'}} \quad (8)$$

where  $\bar{\alpha}^{ss'}$  refers to the effective latent hardening matrix. The latter is essentially affected by the core-diffusion mechanisms, which will be introduced later in this section.

The traveling time  $t_t^s$  is given by  $t_t^s = \lambda^s / v_t$ . Here  $v_t$  is the dislocation traveling velocity. It is assumed to be equal to the shear wave velocity  $v_t \approx C_s = \sqrt{\mu / \rho_0}$  (Austin and McDowell, 2011; Hirth and Lothe, 1983) where  $\rho_0 \approx 6520 \text{ kg} \cdot \text{m}^{-3}$  is the mass density and  $\mu = 42518.52 - 22.185 T(K)$  MPa is the shear modulus for Zr (Moon et al., 2006). It is worth mentioning that the solute dragging mechanism may affect the traveling time of dislocations. However, since the correlation is uncertain, in this work solute dragging is not formulated in the travel time. Instead, its effect on the dislocation motion is accounted for within the waiting time term (see section 4).

The bypass of dislocation-type obstacles corresponds to the bowing-out between the dislocation junctions with the assistance of thermal fluctuation. The waiting time for this thermally-activated process can be expressed using the Kocks-type activation enthalpy law (Austin and McDowell, 2011; Kocks et al., 1975; Lloyd et al., 2014):

$$\frac{1}{t_w^s} = \frac{v^s}{\exp\left(\frac{\Delta G^s}{kT}\right)} \quad (9)$$

where  $k$  is Boltzmann constant;  $T$  denotes the absolute temperature;  $v^s$  is the attack frequency. It is suggested to be associated with the average length of the

vibrating dislocation segments between two pinning points (represented by the mean spacing between obstacles  $\lambda^s$ ) (Granato et al., 1964; Wang et al., 2017):

$$\nu^s = \chi_e C_s / \lambda^s \quad (10)$$

$\chi_e$  is an entropy factor (of the order of 1);  $C_s$  represents the shear wave velocity (speed of sound).  $\Delta G^s$  in Eq. 9 is the activation energy, which is expressed in Kocks et al. (1975) as:

$$\Delta G^s = \begin{cases} \Delta G_0 \left( 1 - \left( \frac{|\tau_{eff}^s|}{\tau_c^s} \right)^p \right)^q & \text{if } |\tau^s| < \tau_c^s \\ 0 & \text{if } |\tau^s| \geq \tau_c^s \end{cases} \quad (11)$$

with  $\Delta G_0$  denotes the thermal activation energy without any external stress applied.  $p$  ( $0 < p \leq 1$ ) and  $q$  ( $1 \leq q < 2$ ) are parameters determining the shape of the obstacles resistance profile (Kocks et al., 1975).  $\tau_{eff}^s$  refers to the effective stress assisting the dislocation to overcome the barriers: it combines the applied resolved shear stress ( $\tau^s$ ) as the driving stress and the added resistance to dislocation motion induced by the diffusion of solute atoms around the dislocation core. The core-diffusion will be introduced below. The kinetic of solute clustering is a classic topic since the 1940s (Cottrell, 1948; Cottrell and Jaswon, 1949). In the 2000s, a series of atomistic studies (Curtin et al., 2006; Olmsted et al., 2006; Picu, 2004; Zhang and Curtin, 2008) were carried out for the edge dislocations in FCC Al-Mg alloy, aiming to reveal the process of dynamic strain aging and anomalous strain rate sensitivity within a certain temperature interval. The proposed theory was later summarized and applied in a rate-dependent constitutive model (Soare and Curtin, 2008a, 2008b). In the core-diffusion model, the solutes tend to diffuse around the core of pinned dislocation. The atomic level simulation performed by Curtin et al. (2006) shows that the binding energy of solutes around an edge dislocation varies between the two sides of the slip plane. The binding energy differential tends to drive the solutes to diffuse from one side of the slip plane to the other. As a consequence, the binding energy between the dislocation and its present position is increased. Denoting the average activation enthalpy for solute transitions as  $\Delta H_c$ , then the transition rate from compression to tension side can be written as:

$$\Gamma_{c-t} = m \nu_0 e^{-(\Delta H_c - \Delta \bar{W})/kT} \quad (12)$$

where  $\Delta \bar{W}$  refers to the average binding energy difference.  $\nu_0$  is the attempt frequency for atomic motion.  $m$  denotes the number of neighbors that each site has on the other side of the slip plane. In the same way, the transition rate from tension to compression side is:

$$\Gamma_{t-c} = m\omega_0 e^{-(\Delta H_c + \Delta \bar{W}/2)/kT} \quad (13)$$

Therefore, the rate of the solute concentration change at time  $t$  is given as:  $\dot{c}_t(t) = m\omega_0 \exp(-(\Delta H_c - \Delta \bar{W}/2)/kT) - m\omega_0 \exp(-(\Delta H_c + \Delta \bar{W}/2)/kT)$ . Considering the initial condition that the solute concentrations on both sides are equal to the one in bulk ( $c_0$ ), one can obtain:

$$\Delta c_t(t) = c_0 \tanh(\Delta \bar{W}/2kT) \left( 1 - \exp\left(-\left(\frac{t}{t_d}\right)^\varphi\right) \right) \quad (14)$$

with

$$t_d = \frac{1}{2m\omega_0 \cosh\left(\frac{\Delta \bar{W}}{2kT}\right) \exp\left(-\frac{\Delta H_c}{kT}\right)} \approx \frac{1}{m\omega_0} \exp\left(\frac{\Delta H_c - \Delta \bar{W}}{2kT}\right) \quad (15)$$

where  $t_d$  represents the scaling time for the core-diffusion process. The power  $\varphi$  is equal to 1, which is derived from the calculation above assuming the solute diffusion enthalpy is uniform across the width of the core. According to Soare and Curtin (2008a), for any migration enthalpy distribution, an approximate solution can be obtained by using  $\varphi < 1$ . The change in the binding energy is then expressed as:

$$\Delta E^{core}(t) = \Delta c_t(t) N \Delta \bar{W} \quad (16)$$

Or, in a more common way:

$$\Delta E^{core}(t) = \Delta E_\infty^{core} \left( 1 - \exp\left(-\left(\frac{t}{t_d}\right)^\varphi\right) \right) \quad (17)$$

where  $\Delta E_\infty^{core} = c_0 N \Delta \bar{W} \tanh(\Delta \bar{W}/2kT)$  is the saturation value for the binding energy change.  $N$  in Eq. 16 is the number of atoms for unit length of dislocation segment in a core of width  $\bar{w}$ .

In the core-diffusion model, the increase in the binding energy tends to affect the dislocation mobility by affecting both, the pinned and the pinning dislocations. In the former case, it will further bind the pinned dislocation to its current position, and an extra stress is required for the dislocation to unpin from the obstacles. This stress, denoted as  $\Delta \tau_m^s$ , is proportional to  $\Delta E^{core}$  for an uniform distribution of migration enthalpy, but not necessarily so otherwise. However, Soare and Curtin (2008a) restore the proportional relationship for both cases for the sake of simplicity. Notice that the solute diffusion occurs while the dislocation is waiting at obstacles before the bypass. Thus aging time in this mechanism should refer to the local aging time, which

depends on the waiting time. Notice that the local aging time  $t_{a,local}^s$  should not exceed the current duration of the test (creep time  $t_c$ ). Therefore:

$$t_{a,local}^s = \begin{cases} t_w^s & (\text{if } t_w^s < t_c) \\ t_c & (\text{if } t_w^s > t_c) \end{cases} \quad (18)$$

and the  $\Delta\tau_m^s$  term can be written as:

$$\Delta\tau_m^s(t_{a,local}^s) = \frac{\alpha\Delta E^{core}(t_{a,local}^s)}{\bar{w}b^s} = \frac{\alpha\Delta E_{\infty}^{core}}{\bar{w}b^s} \left( 1 - \exp\left(-\left(\frac{t_{a,local}^s}{t_d}\right)^{\varphi}\right) \right) \quad (19)$$

where  $\alpha$  is a coefficient accounting for the energy variation along the core. In the present work,  $\Delta\tau_m^s$  and  $t_{a,local}^s$  are calculated for each sub-material point.

The other effect of  $\Delta E^{core}$  is that the effective junction strength will be increased. This mechanism was proposed by Picu (2004), where the junction strength (Lomer-Cottrell lock) between a mobile and a clustered forest dislocation is computed with different binding energies. Here  $\Delta E^{core}/A$  is considered as a normalized binding energy due to the core-diffusion process, where  $A = 3\mu b^2/4\pi(1-\nu)$  is the energy per unit length of edge dislocation segment,  $\nu \approx 0.34$  denotes the Poisson ratio, and  $\mu$  is the shear modulus. The results show that the stress required for unpinning ( $\Delta\tau_l^s$ ) increases linearly with  $\Delta E^{core}/A$ , and remains constant after  $\Delta E^{core}/A$  reaches a certain value. The principle is that the forest dislocation tends to move from its original location to form a longer junction segment which will facilitate the unzipping process. However, this is impeded for a high value of the binding energy  $\Delta E^{core}/A$  value, in which case the forest dislocation remains at its original position at all stress levels, and the bypass mechanism switches from junction unzipping to mobile dislocation instability. It is essential to mention that this process depends on the aging of the dislocations that play the role of obstacle, not the dislocations attempting to unpin and glide. A moving dislocation may encounter any other dislocation with different aging history. Therefore the junction strength should be determined considering the aging effect in all the sub-material points. In the present work, the original formulation of Soare and Curtin (2008a) is adapted and the effect of  $\Delta E^{core}$  is included in the effective latent hardening matrix for each sub-material point:

$$\bar{\alpha}_{local}^{ss'} = \alpha^{ss'} \left( 1 + \frac{\chi\Delta E^{core}(t_{a,local}^s)}{A} \right)^2 \quad (20)$$

where  $\chi$  is a pre-factor linearly linking the binding energy to the junction strength.  $\alpha^{ss'}$  is the latent hardening matrix describing the dislocation-dislocation interaction

strength without any contribution from the core-diffusion process.  $t_{a,local}^{s'}$  denotes the local aging time of dislocations on slip system  $s'$ . Similar to Eq. 3, the effective latent hardening matrix in one grain can be calculated as a mean value:

$$\bar{\alpha}^{ss'} = \int_{-\infty}^{\infty} \bar{\alpha}_{local}^{ss'} P(\tau^{s'} - \bar{\tau}^{s'}) d\tau^{s'} \quad (21)$$

The mean line tension resistance acting on a pinned dislocation is assumed to be inversely proportional to mean interspacing between obstacles. Therefore, we have:

$$\Delta\tau_l^s = \mu b^s \sqrt{\sum_s \bar{\alpha}^{ss'} \rho^{s'}} \quad (22)$$

Notice that the solutes may also pin the dislocations (solute pinning) and thus affect the line tension. However, in the present work this effect is effectively considered in the Critical Resolved Shear Stress (CRSS) as shown later in Eq. 24.

As described above,  $\Delta\tau_m^s$  and  $\Delta\tau_l^s$  are the resistances acting on a pinned dislocation. Therefore, the effective driving stress ( $\tau_{eff}^s$ , Eq. 11) for the bypass process is expressed as:

$$\tau_{eff}^s = \tau^s - \Delta\tau_m^s - \Delta\tau_l^s \quad (23)$$

In Eq. 11,  $\tau_c^s$  represents the Critical Resolved Shear Stress (CRSS). It is known that the dislocation core structure is a function of temperature. As a result, varying the temperature may affect the interaction between the dislocation and the obstacle, which leads to changes in the stress barrier to unpin. Therefore, in the present work  $\tau_c^s$  is considered as temperature-dependent:

$$\tau_c^s = \tau_0^s + \tau_s \quad (24)$$

where  $\tau_0^s$  is lattice friction at the creep temperature without the presence of solutes, which can be obtained from single crystal tests or atomistic simulations;  $\tau_s$  is the contribution from the pinning of solute atoms. The temperature dependence of  $\tau_0^s$  and  $\tau_s$  will be discussed in section 3.

## 2.2 Dislocation density evolution

The dislocation density evolution plays a key role in the present thermal creep model. It is responsible for capturing the rate changes in the primary creep stage. It will also affect the variance in the stress distribution (Eq. 5) and hence the mean dislocation mobility. The law for the dislocation density evolution is introduced in this section. Notice that all dislocations in this thermal creep model are considered as mobile, with their actual mobility governed by the local stress state. The forest dislocations

reported in experiments are effectively immobilized due to the fact that local stresses are insufficient to overcome the resistance. The processes considered in this model for  $\dot{\rho}^s$  are dislocation generation ( $\dot{\rho}_g^{s,+}$ ) and dynamic recovery ( $\dot{\rho}_a^{s,-}$ ). The evolution law is written as:

$$\dot{\rho}^s = \dot{\rho}_g^{s,+} - \dot{\rho}_a^{s,-} \quad (25)$$

The generation rate is related to the area swept by the traveling dislocations. The term  $\dot{\rho}_g^{s,+}$  is determined by a commonly used expression (Kitayama et al., 2013; Wen et al., 2016, 2015):

$$\dot{\rho}_g^{s,+} = \frac{k_1}{b^s \lambda^s} |\bar{\gamma}^s| \quad (26)$$

Cross-slip and climb (Estrin, 1998; Nes, 1997) are suggested to be the essential mechanisms for the dynamic recovery process, through which one dislocation is able to move to another slip plane and annihilate with another dislocation with opposite Burgers vector. In the well-known Kocks-Mecking law (Beyerlein and Tomé, 2008; Estrin, 1998; Kocks and Mecking, 2003; Mecking and Kocks, 1981), the annihilation term is expressed as:

$$\dot{\rho}_a^{s,-} = f \rho^s |\bar{\gamma}^s| \quad (27)$$

where  $f$  is the recovery parameter which is a function of temperature and shear rate. Estrin (1998) suggested that the strain rate sensitivity of  $f$  depends on the dominant annihilation mechanism. The general expression for  $f$  proposed by Estrin (1998) is:

$$f = k_2 \left( \frac{\dot{\epsilon}_0}{\dot{\epsilon}} \right)^{\frac{1}{n_0}} \quad (28)$$

where  $n_0$  is a strain rate sensitivity parameter and  $\dot{\epsilon}_0$  refers to the reference strain rate. Notice that the values of  $n_0$  and  $\dot{\epsilon}_0$  are related to the temperature, as well as the relative activities of climb or cross-slip mechanisms (Estrin, 1998).

### 2.3 Coble creep

Besides the dislocation motion, the plastic deformation in polycrystals may take place by the mass transport of vacancies across the grain (Nabarro-Herring) or along the grain boundaries (Coble). These diffusional creep mechanisms are relevant at high-temperature and/or low-stress conditions, and dictate a creep regime with stress exponent close to 1. The competition between Nabarro-Herring creep and Coble creep is associated with the temperature and grain size. For the material and test conditions (500°C-600°C, 8.5µm of grain size) involved in the studies of Kombaiah and Murty (2015a, 2015b), Coble creep is the governing mechanism. The creep law proposed by

Coble (1963) is written as:

$$\dot{\epsilon}_{ij}^{coble} = \frac{\alpha_{gb} D_{gb} \delta_{gb} \Omega}{\pi \lambda_g^3 kT} \sigma_{ij} \quad (29)$$

where  $\alpha_{gb} = 148$  (Coble, 1963) is a constant;  $\delta_{gb}$  denotes the grain boundary width;  $\Omega$  is the atomic volume;  $\lambda_g$  refers to the grain size;  $D_{gb}$  is the grain boundary diffusion coefficient that can be expressed using the well-known Arrhenius relation:

$$D_{gb} = D_{gb,0} \exp\left(-\frac{Q_{gb}}{kT}\right) \quad (30)$$

with  $D_{gb,0}$  and  $Q_{gb}$  denote the pre-exponential factor and the effective activation energy for grain boundary diffusion. Because some of the parameters that appear in the Coble creep law are affected by the presence of impurities and are not known for Zircaloy-4, here we adopt an empirical approach. We reduce Eqs. 29 and 30 to a simple form where the parameters  $A^{coble}$  and  $Q_{gb}$  can be obtained by backfitting to the experimental data of Kombaiah and Murty (2015b) in the Coble creep regime:

$$\dot{\epsilon}_{ij}^{coble} = \frac{A^{coble} \sigma_{ij}}{T} \exp\left(-\frac{Q_{gb}}{kT}\right) \quad (31)$$

### 3 Simulation conditions and parameter calibration

#### 3.1 Simulation conditions

The parameters involved in the simulations are discussed in this section. The simulations mainly aim to reproduce the creep behavior of Zircaloy-4 at 500°C, 550°C and 600°C reported in Kombaiah and Murty (2015a, 2015b). The constant strain-rate tensile tests are carried out within the temperature interval of 200°C-600°C to analyze the anomaly in strain rate sensitivity. In this work, the affine interaction in the VPSC framework is chosen to describe the interaction between the grain and the surrounding effective medium (Lebensohn et al., 2007; Masson et al., 2000; Wang et al., 2010). A rolling texture of Zr alloy with 100 grains (Fig. 2) is used as input and the tensile tests are performed along the rolling direction to replicate the loading condition of Kombaiah and Murty (2015a, 2015b).

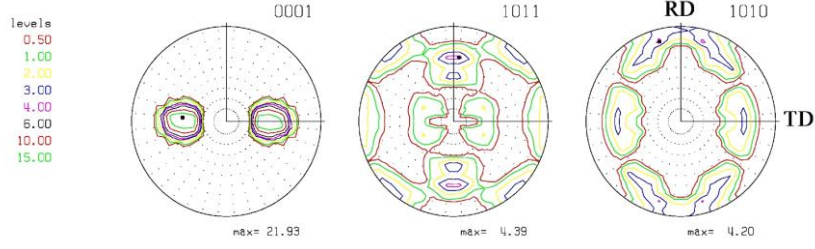


Fig. 2. Initial texture of rolled Zr alloy. RD and TD represent rolling and transverse directions, respectively.

The slip systems considered in our simulations are prismatic  $\langle a \rangle$ , basal  $\langle a \rangle$ , pyramidal  $\langle a \rangle$  and pyramidal  $\langle c+a \rangle$ . The slip and twinning activities in Zr have been investigated in many works. Zr and its alloys are HCP metals with  $c/a$  ratio of 1.594. Generally, prismatic  $\langle a \rangle$  type slip systems are favored, whereas the  $\langle c+a \rangle$  type is only detected occasionally. Activation of basal slip is negligible at low temperature but has been observed above 800K (Akhtar, 1973a; Beyerlein and Tomé, 2008). Single crystal tests (Akhtar, 1975, 1973a) on pure Zr (impurity  $\approx 120$ ppm) show that the lattice friction stress for prismatic slip is less than 10MPa in the temperature interval of 800K-1100K while that for basal slip is slightly higher but within the same order of magnitude. Pyramidal  $\langle c+a \rangle$  slip can also be activated but with critical stress 10 to 20 times higher than the prismatic slip. Besides, pyramidal  $\langle a \rangle$  is also considered in the simulations since cross-slip of screw segment from prismatic plane to pyramidal  $\langle a \rangle$  and basal planes has been reported for Zr alloys (Caillard et al., 2015; Onimus et al., 2013).  $\{10\bar{1}2\}$  tensile twinning and  $\{11\bar{2}2\}$  compressive twinning are excluded from this work as their activations are suppressed at elevated temperatures (Beyerlein and Tomé, 2008; Kanitpanyacharoen et al., 2012).

### 3.2 Parameter calibration

In the Zr alloy used for comparison, the initial dislocation density is reported to be low (of order  $10^{12} \text{ m}^{-2}$ ), and most of the dislocations are on the prismatic slip plane (Caillard et al., 2015; Kombaiyah and Murty, 2015a, 2015b; Moon et al., 2006; Morrow et al., 2016, 2013). To comply with this observation, the initial dislocation density is set to be  $2.4 \cdot 10^{11} \text{ m}^{-2}$  for each prismatic slip system and  $0.14 \cdot 10^{11} \text{ m}^{-2}$  for each basal, pyramidal  $\langle a \rangle$  and pyramidal  $\langle c+a \rangle$  system. Therefore the total initial dislocation density is  $\approx 10^{12} \text{ m}^{-2}$ . In Eq. 5, the scaling parameter  $\eta$  is set to be  $3.16 \cdot 10^{-5} \text{ MPa/m}$  by back-fitting to the experimental data. As a result, the initial variance determined from Eq. 5 is  $V \approx 11.4 \text{ MPa}$ . The latent hardening matrix  $\alpha^{ss'}$  for Zr is unknown from literature. Hence  $\alpha^{ss'}$  values reported in Wen et al. (2015)

for HCP Mg are employed in this study. The parameters  $\Delta G_0$ ,  $\chi_e$ ,  $p$  and  $q$  are obtained by reverse-fitting to experimental data within reasonable ranges ( $\chi_e \approx 1$  (Wang et al., 2017);  $0 < p \leq 1$  and  $1 \leq p < 2$  (Kocks et al., 1975)).

The dislocation density evolution parameters  $k_1$ ,  $k_2$  and  $n_0$  are calibrated according to the experimental data. The annihilation parameter  $k_2$  and the strain rate sensitivity parameter  $n_0$  in the dislocation dynamic recovery term are dependent on the annihilation mechanisms (climb or cross-slip) (Estrin, 1998).  $n_0$  is suggested to be a constant (around 3-5) if climb is the dominant mechanism in dynamic recovery. Otherwise (cross-slip controlled process), its value should be higher. In this work,  $n_0$  is chosen to be 20 and  $k_2$  varies with temperature, implying that climb is not the dominant mechanism, which will be discussed in the following sections. The value of  $k_2$  is obtained by fitting to the experimental data of Kombaiah and Murty (2015a, 2015b). The determined  $k_2$  values are 24, 26 and 28 for 500°C, 550°C and 600°C, respectively. It appears that  $k_2$  shows linear-dependent on temperature within this interval. Therefore, an empirical expression for  $k_2$  is proposed as  $k_2 = T/25\text{K} - 6.92$ . The Coble creep related parameters  $A$  and  $Q_{gb}$  (Eq. 31) are determined to be  $8 \cdot 10^4 \text{ K} \cdot \text{Mpa}^{-1} \cdot \text{s}^{-1}$  and 1.8eV respectively through back-fitting. All the parameters mentioned above are listed in Table 1.

The parameters related to the core-diffusion mechanisms are listed in Table 2. It is worth mentioning that the primary aim here is to demonstrate that the general mathematic form of the core-diffusion model is capable of describing the behavior of Zircaloy-4. Determining accurately the parameters related to the core structure and solute diffusion would require atomistic analysis, which is out of the scope of this study. The dislocation core structure in HCP material is complex compared to the FCC Al-Mg alloy studied in Soare and Curtin (2008a) and the core diffusion process in Zircaloy-4 has not been analyzed in detail. In this case, the core-related parameters  $\bar{w}$ ,  $m$  and  $N$  are set to be  $7.5b$ , 3 and  $2\bar{w}/b^2\sqrt{3}$ , which are the values for FCC materials (Curtin et al., 2006). In the present work, the solute concentration is set to 2%

based on the chemical composition given in Kombaiah and Murty (2015a, 2015b). The reference core-diffusion time  $t_d$  is an essential variable in this work. The parameters involved in the calculation of  $t_d$  are calibrated with the experimental data.  $t_d$  controls not only where the transition between the power law regions occurs, but also at which temperature the anomalous SRS appears. The role of  $t_d$  will be discussed in the following sections. The power  $\varphi$  is suggested to be 1 if the solute diffusion enthalpy is uniform across the width of the core and  $\varphi < 1$  if otherwise.  $\varphi = 1$  is selected in this work due to the lack of information about core-diffusion in Zr alloys.

Tab. 1. Parameters used for the Zircaloy-4 in this work

Parameters	Zircaloy-4	
$b^s$ (magnitude of Burgers vector)	2.231·10 <sup>-10</sup> m (prismatic, basal and pyramidal<a> 6.077·10 <sup>-10</sup> m (pyramidal<c+a>)	(Beyerlein and Tomé, 2008) <sup>#</sup>
$\mu$ (shear modulus)	42518.52MPa·T-22.185MPa/K	(Moon et al., 2006) <sup>#</sup>
$\eta$ (scaling parameter)	1.14·10 <sup>-5</sup> MPa/m	
$\Delta G_0$ (zero-stress activation energy for dislocations)	2.4 eV	
$p$ (exponent parameter)	0.8	(Kocks et al., 1975)*
$q$ (exponent parameter)	1.1	(Kocks et al., 1975)*
$\chi_e$ (entropy factor)	1	(Wang et al., 2017) <sup>#</sup>
$\rho_0^s$ (initial dislocation density in the cell)	2.4·10 <sup>11</sup> m <sup>-2</sup> (prismatic) 1.4·10 <sup>10</sup> m <sup>-2</sup> (basal, pyramidal<a> and pyramidal<c+a>)	(Moon et al., 2006; Morrow et al., 2013)*
$k_1$ (material constant)	0.001	
$k_2$ (annihilation parameter)	$k_2 = T/25\text{K} - 6.92$	
$n_0$ (annihilation strain rate sensitivity)	20	
$\dot{\epsilon}_0$ (reference strain rate)	1 s <sup>-1</sup>	
$A^{coble}$ (Coble creep parameter)	8·10 <sup>4</sup> K·Mpa <sup>-1</sup> ·s <sup>-1</sup>	
$Q_{gb}$ (Activation energy for grain boundary diffusion)	1.8 eV	

<sup>#</sup> indicates the value of the parameter is taken from the given reference; \* indicates the value of the parameter is estimated or back-fitted from experimental data within the range mentioned in the given reference; the remaining parameters are back-fitted from experimental data.

Tab. 2. Core-diffusion related parameters for Zircaloy-4

Parameters	Zircaloy-4
$m$	3
$\varphi$	1
$\Delta H_c$	1.9eV
$\Delta \bar{W}$	0.13eV
$\nu_0$	$1 \cdot 10^{13} s^{-1}$
$\bar{w}$	1.86 nm
$\chi$	20
$\alpha$	1

### 3.3 Temperature-dependence of the CRSS

In the model introduced above, some parameters are temperature-dependent, such as the CRSS which includes the lattice friction without the presence of solute atoms on each slip system ( $\tau_0^s$ ) and the contribution from the pinning of solute atoms ( $\tau_s$ ). The former can be determined from single crystal tests on pure Zr. In the present work, the values of  $\tau_0^s$  are expressed using simple mathematic expressions that roughly represent the single crystal test data summarized from literatures. For prismatic slip, Akhtar et al. (Akhtar, 1975; Akhtar and Teghtsoonian, 1971) reported the measured lattice friction from 300K to 1100K. The data are plotted in Fig. 3a. Notice that  $\tau_0^s$  generally decreases with increasing temperature but a plateau appears between around 600K and 800K. For the low-temperature regime, an empirical fitting is expressed as:

$$\tau_0^{pris} = 21 \text{ MPa} \cdot \exp\left(-\frac{T}{500 \text{ K}}\right) \quad (32)$$

and for high-temperature regime:

$$\tau_0^{pris} = 586 \text{ MPa} \cdot \exp\left(-\frac{T}{183.4 \text{ K}}\right) \quad (33)$$

The empirical fittings are also plotted in Fig. 3a. For the intermediate temperature interval,  $\tau_0^{pris} = 6.3 \text{ MPa}$  is assumed to describe the plateau (dash line).

Measured  $\tau_0^s$  for basal slip are reported only above 820K (Akhtar, 1973b). For temperature lower than that, the values are obtained by empirical fitting assuming  $\tau_0^s$

decays exponentially with temperature (see Fig. 3b) as:

$$\tau_0^{basal} = 25000 \text{ MPa} \cdot \exp\left(-\frac{T}{115 \text{ K}}\right) \quad (34)$$

This rough estimate may lead to inaccuracy in the lower temperature region. However this should not affect the simulation significantly since the basal slip is almost inactive below 800K (Akhtar, 1973a; Beyerlein and Tomé, 2008).

$\tau_0^s$  for pyramidal  $\langle c+a \rangle$  is measured in Akhtar (1973a) for temperature above 850K through compression tests along the c-axis. For lower temperature, Beyerlein and Tomé (2008) proposed an exponential expression for  $\tau_0^s$  of pyramidal  $\langle c+a \rangle$  below 450K based on the model estimates at certain temperatures. It can be seen that both sets of data (plotted in Fig. 3c) show an exponential decrease with the increasing temperature. However, there is a gap between 450K and 850K where the values of  $\tau_0^s$  are not available. One may expect that a plateau exists as for prismatic slip. In this work, the data above 850K is empirical fitted using the expression:

$$\tau_0^{pyra\langle c+a \rangle} = 5100 \text{ MPa} \cdot \exp\left(-\frac{T}{200 \text{ K}}\right), T \geq 850 \text{ K} \quad (35)$$

whereas the ones below 450K are given in Beyerlein and Tomé (2008) as:

$$\tau_0^{pyra\langle c+a \rangle} = 722.5 \text{ MPa} \cdot \exp\left(-\frac{T}{200 \text{ K}}\right), T \leq 450 \text{ K} \quad (36)$$

From Eqs. 35 and 36,  $\tau_0^{pyra\langle c+a \rangle}$  is around 76MPa at both 450K and 850K. Therefore,

for the sake of simplicity, the values of  $\tau_0^{pyra\langle c+a \rangle}$  are assumed to be equal to 76MPa in this interval (dash line in Fig. 3c). Pyramidal  $\langle a \rangle$  slip mode is also accounted for in this study. As for basal slip, the activity of pyramidal  $\langle a \rangle$  slip mode is low for the temperature range involved but cross-slip from prismatic planes are observed. Thus here the lattice friction for pyramidal  $\langle a \rangle$  is simply treated as equal to basal mode.

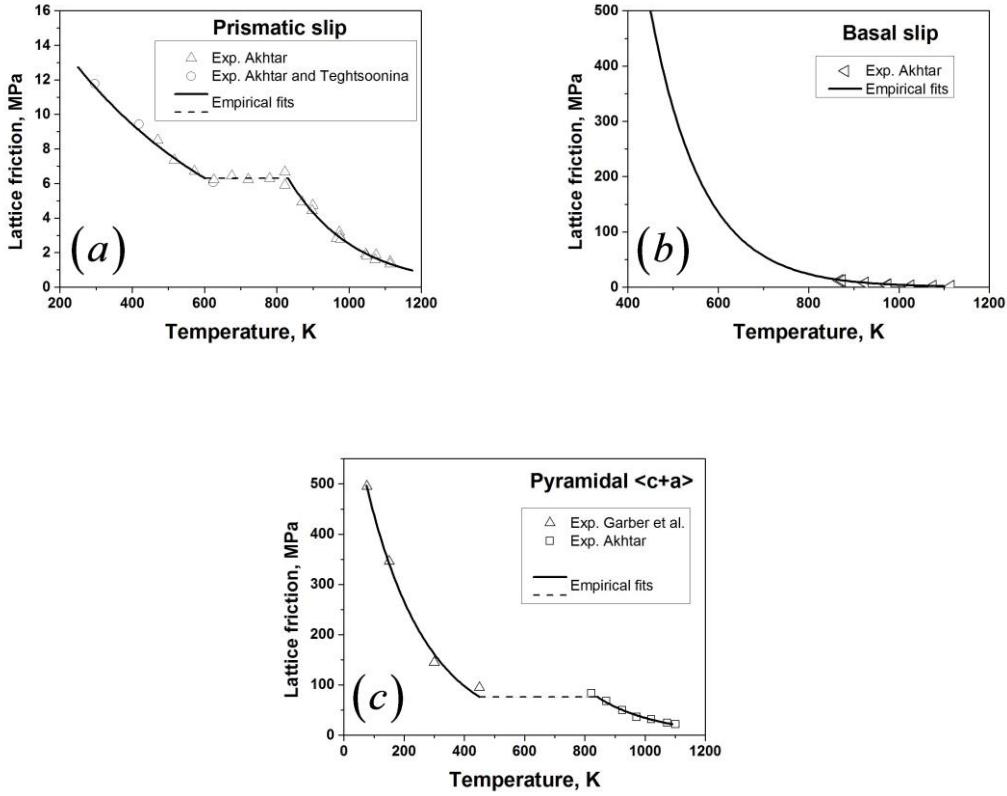


Fig. 3. Dependence of lattice friction with temperature in pure Zr for: (a) prismatic slip, experimental data from Akhtar (1975) and Akhtar and Teghtsoonian (1971); (b) basal slip, experimental data from Akhtar (1973b); (c) pyramidal  $\langle c+a \rangle$  slip, experimental data from Akhtar (1973a) and Garber et al (1963)

The  $\tau_s$  term in Eq. 24 represents the hardening contribution due to the pinning of dislocations by solute atoms. When a dislocation is traveling within the random field of solutes, it interacts with these point obstacles, which results in extra resistance for the dislocation to glide. Friedel (1956) analyzed this resistance for strong-pinning, which corresponds to the stress required for bowing out between the pinning points (Fleischer, 1966; J. Friedel, 1956). Derived from Friedel's theory, Labusch (1970) proposed a law assuming that the strength of each solute alone is insufficient to pin completely the dislocation (Leyson and Curtin, 2013). Notice that laws proposed by Friedel and Labusch describe the solute strengthening at 0K. Many investigations have been carried out to study the temperature-dependence of solute pinning in Cubic materials (i.e. Leyson and Curtin, 2016; Zaiser, 2002). However, most of them focus on low and moderate temperature regimes. Moreover, the solute strengthening in Zircaloy-4 is rather complicated due to the presence of multiple types of impurity and the complex HCP core-structure. Detailed atomistic-level simulations are necessary to fully understand this process. In theory,  $\tau_s$  should approach the value determined from the laws of Friedel or Labusch when the temperature is close to 0K, whereas it should vanish gradually when the temperature is increased to a value where the

solutes cannot pin the dislocations anymore. However, due to the lack of information on this subject, the value  $\tau_s$  is assumed to be equal for all slip systems and determined by fitting the experimental data of Kombaiah and Murty (2015a, 2015b) for each temperature (148MPa, 127MPa and 110MPa for 500°C, 550°C and 600°C, respectively).  $\tau_s$  values for the 200-500°C interval, which are needed for the analysis of strain rate sensitivity (SRS) in section 4, is obtained using an exponential expression fitted to values in the 500-600°C, as:

$$\tau_s = 3100\text{MPa} \cdot \exp\left(-\frac{T}{230\text{K}}\right) + 40.5\text{MPa} \quad (37)$$

The data calculated using Eq. 37 are plotted in Fig. 4.

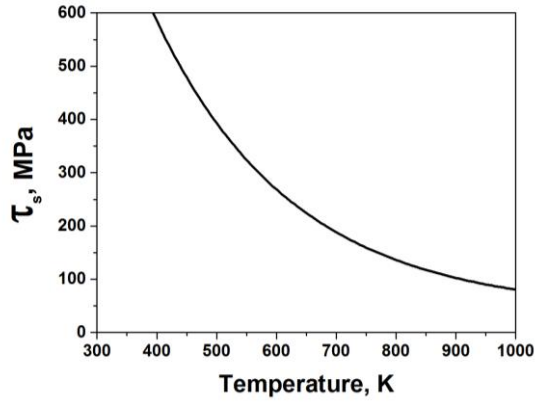


Fig. 4.  $\tau_s$  values used in the simulations obtained using Eq. 37.

## 4 Simulation results

The steady stage creep rates are measured by Kombaiah and Murty (2015a, 2015b) at 500°C, 550°C and 600°C, and the tensile stress ranges from 15MPa to 170MPa (summarized in Fig. 1). These results can be classified into three regions: low-stress zone with creep rates almost linearly dependent on the applied stress (Coble creep regime), intermediate stress zone obeying the power law relationship with  $n \approx 4$ , and high-stress zone with  $n \approx 9$ . Fig. 5 illustrates schematically how the proposed model captures the fast transient from  $n \approx 4$  to  $n \approx 9$  regime. In Fig. 5, the predicted initial creep rates (creep rate at the first step of simulation) using the core-diffusion model (solid lines) are compared to the results with  $\Delta\tau_m^s = 0$  (no core-diffusion) and  $\Delta\tau_m^s = \Delta\tau_{m,\infty}^s$  (saturated atmosphere around the core), respectively. First, it is worth mentioning that without any contribution from solute effects, the predicted creep rates are exponential functions of stress due to the incorporation of the classic Kocks-type activation enthalpy law (Eq. 9). Moreover, the aging time-controlled  $\Delta\tau_m^s(t_{a,local}^s)$  also plays an essential role here. Specifically, it allows for an accelerated increase in creep rate with imposed stress. At low stress the waiting time is high and the solutes

have sufficient time to diffuse around the core, resulting in a high unpinning resistance. According to Eq. 19, the  $\Delta\tau_m^s(t_{a,local}^s)$  term is close to its maximum value. With increasing stress, the waiting time tends to decrease, which leads to a lower  $\Delta\tau_m^s(t_{a,local}^s)$ . As shown in Fig. 5, this mechanism tends to further increase the ‘effective’ power  $n$  at high stress, which seems to provide a behavior closer to the experimental data as illustrated in Fig. 6. Notice that the other core-diffusion related term,  $\Delta\tau_l^s$ , has a very limited effect on creep when  $\chi=20$  due to the low dislocation density considered in the simulations (see section 5 for details).

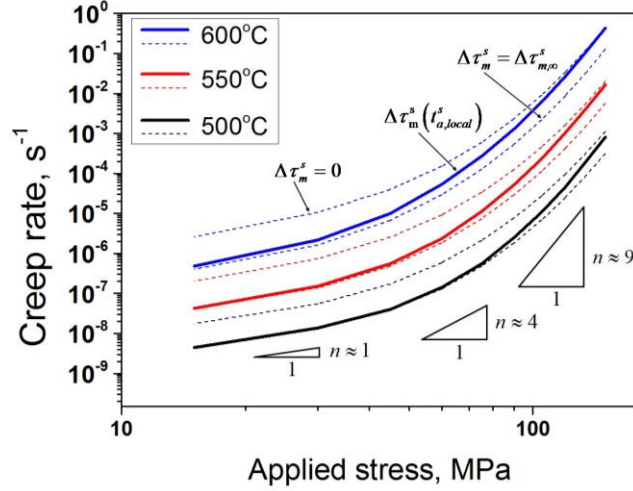


Fig. 5. Predicted initial creep rates at 500, 550 and 600°C demonstrating the role of the local aging time-dependent term  $\Delta\tau_m^s$ . Results from the core-diffusion model with

$\Delta\tau_m^s(t_{a,local}^s)$  (solid lines) are compared with using  $\Delta\tau_m^s = 0$  (upper dash lines) and

$$\Delta\tau_m^s = \Delta\tau_{m,\infty}^s \text{ (lower dash lines)}$$

The steady-state creep rates, predicted using the core-diffusion theory, are presented in Fig. 6. The predicted results are the estimated saturation values from the creep rate-creep time curves. From Fig. 6 we can see that the experimental trends in all power law regimes are generally captured. The creep rates at lower stress are mainly controlled by Coble creep, which will be discussed below in detail. Kombaiah and Murty (2015a, 2015b) report creep rate and creep strain evolution for two tests: 500°C and 129MPa; 550°C and 60.6MPa. These results are captured well in the simulations as shown in Fig. 7. The predicted creep rate and creep strain curves for other cases are shown in Figs. 8-10 with the horizontal dash lines representing the measured steady-state creep rates. Results with and without considering Coble creep are also presented in some cases to analyze its effects. As expected, the relative contribution of the Coble creep mechanism is large and needs to be included in the low-stress regime, and becomes gradually less relevant with increasing stress. Notice that the parameters related to  $\dot{\epsilon}^{coble}$  do not vary significantly during the thermal creep process and hence the Coble creep rate remains quasi-constant. At low-stress ( $\leq 40$ MPa), the decrease of creep rate in the primary stage is dislocation driven creep. As the dislocation motion

induced creep rate decreases because the dislocation density decreases, a steady-state stage is achieved controlled by the Coble creep rate. This indicates that while the Coble creep dictates the steady-state creep rate at  $n \approx 1$  regime, the contribution of dislocation driven creep at primary stage should not be ignored.

Although the steady-state creep behaviors in  $n \approx 4$  and  $n \approx 9$  regimes are well reproduced as illustrated in Fig. 6, some discrepancies are still apparent. Besides the inaccuracy in the parameter calibrations, one possible source of error is associated with the criterion of steady-state. In experiments, the identification of the steady state creep regime is rather ambiguous. The steady-state creep rate (also reported as minimum creep rate in some cases) is affected by material failure after certain amount of strain (Basirat et al., 2012; Gaffard et al., 2005), which are out of the scope of this work. In other word, while the predicted steady-state creep rates in Fig. 6 are achieved through the saturation of dislocation densities, the experimental ones result from various coupled mechanisms. To better understand the creep process, more creep rate vs. time curves are needed with a clear presence of the transition between primary creep and steady-state regimes.

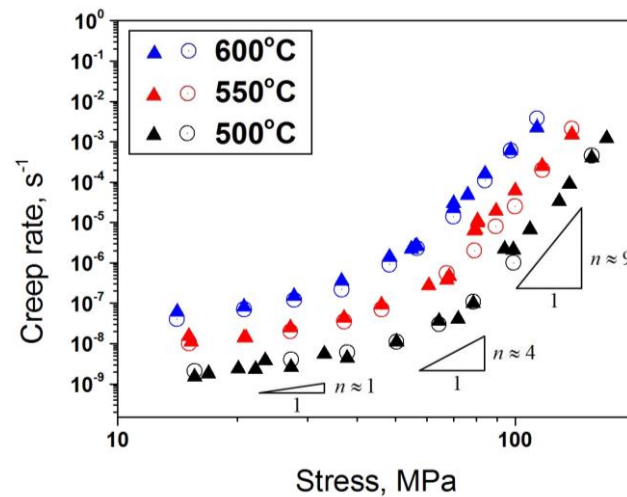


Fig. 6. Comparison between predictions and experimental data. Triangles represent the experimental steady-state creep rates in Kombaiah and Murty (2015a, 2015b); circles represent the predicted saturation creep rates.

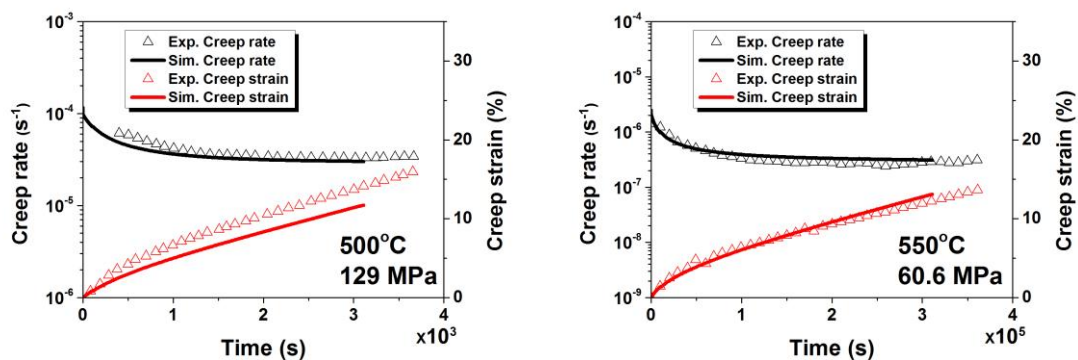


Fig. 7. Predicted creep rate and creep strain for Zircaloy-4 for 129MPa (500°C) and 60.6MPa (550°C). Experimental data from Kombaiah and Murty (2015a, 2015b).

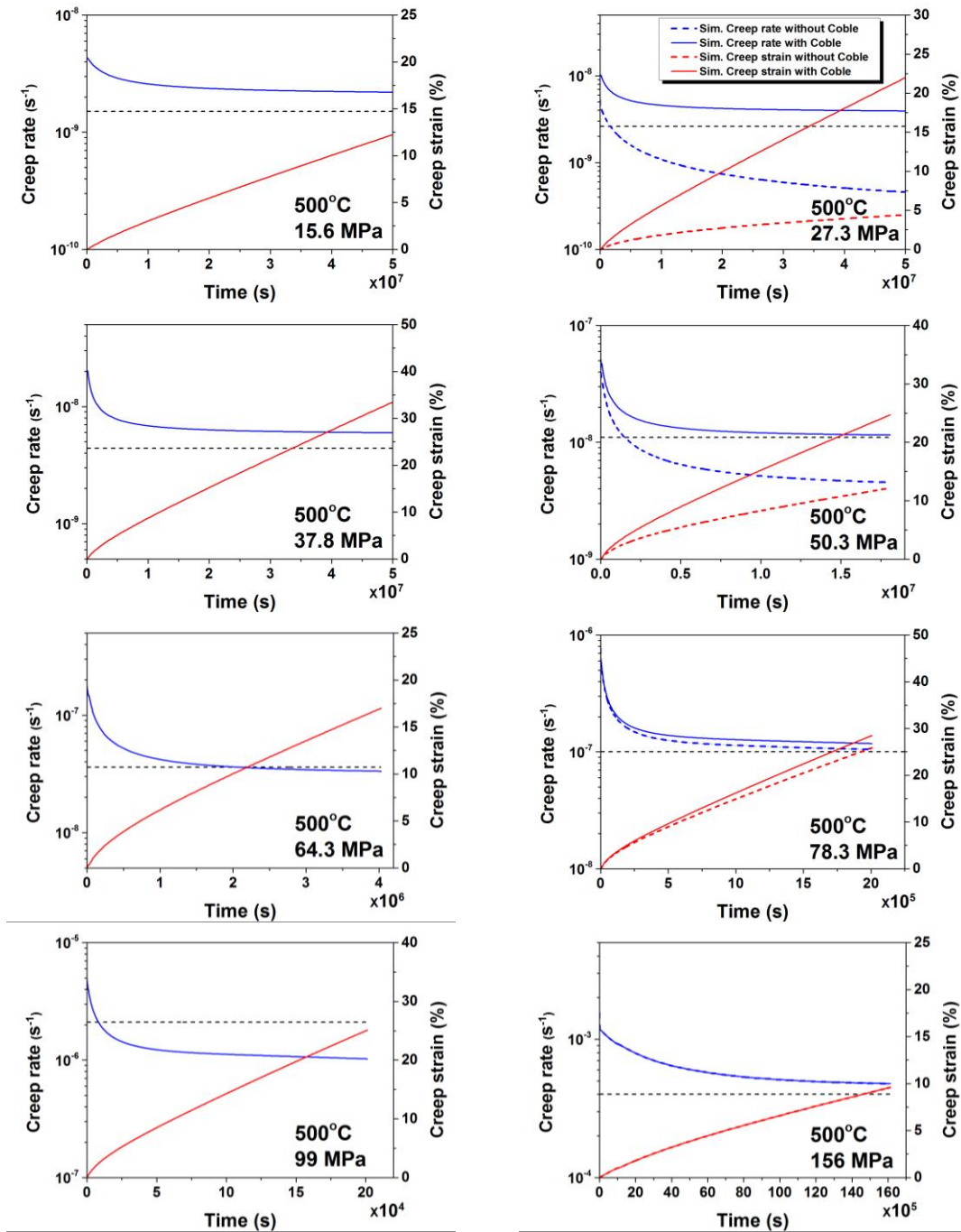


Fig. 8. Predicted creep rate and creep strain for Zircaloy-4 at 500°C for various stresses. Horizontal dash lines represent the measured steady-state creep rate in Kombaiah and Murty (2015a, 2015b).

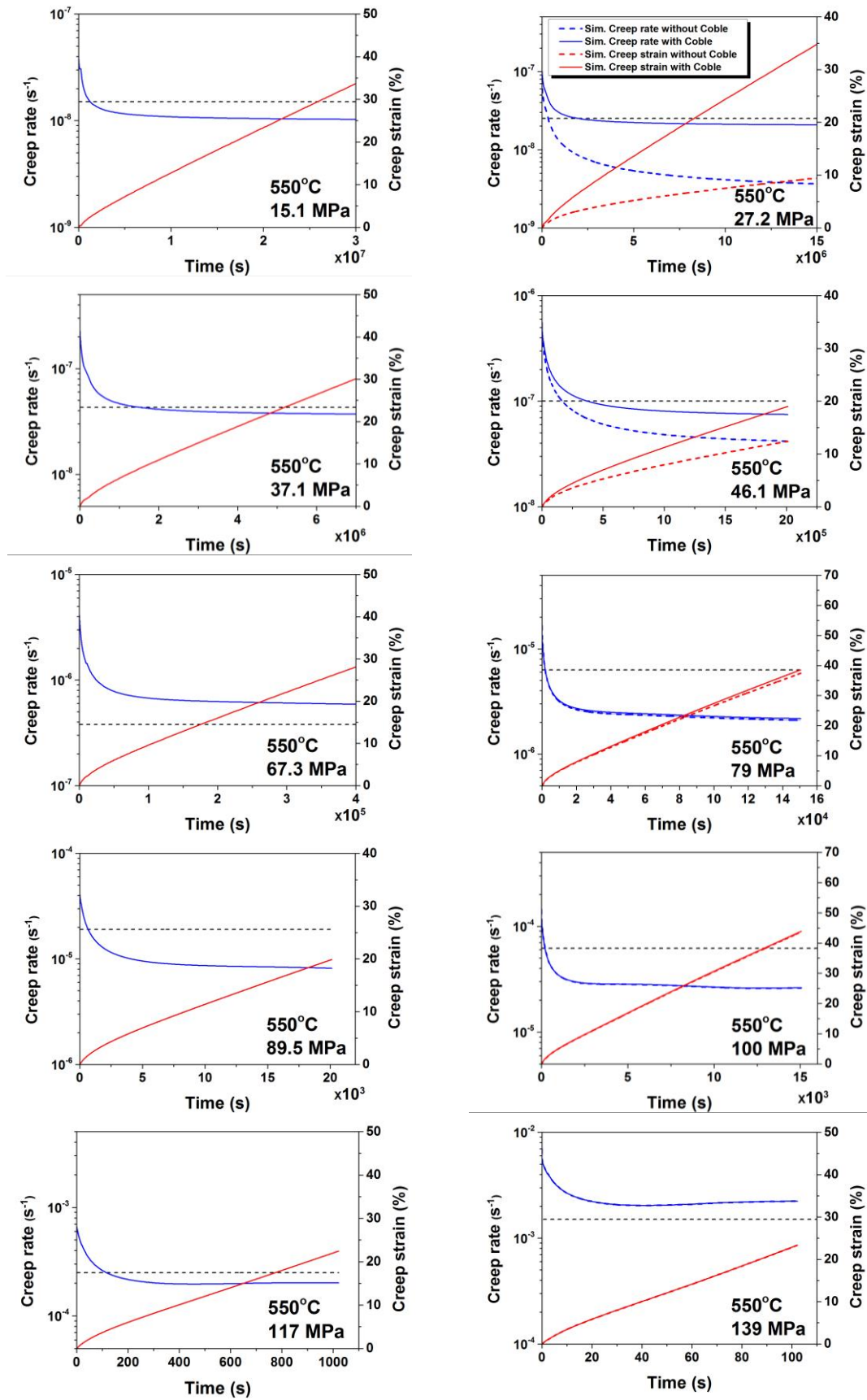


Fig. 9. Predicted creep rate and creep strain for Zircaloy-4 at 550°C for various stresses. Horizontal dash lines represent the measured steady-state creep rate in Kombaiah and Murty (2015a, 2015b).

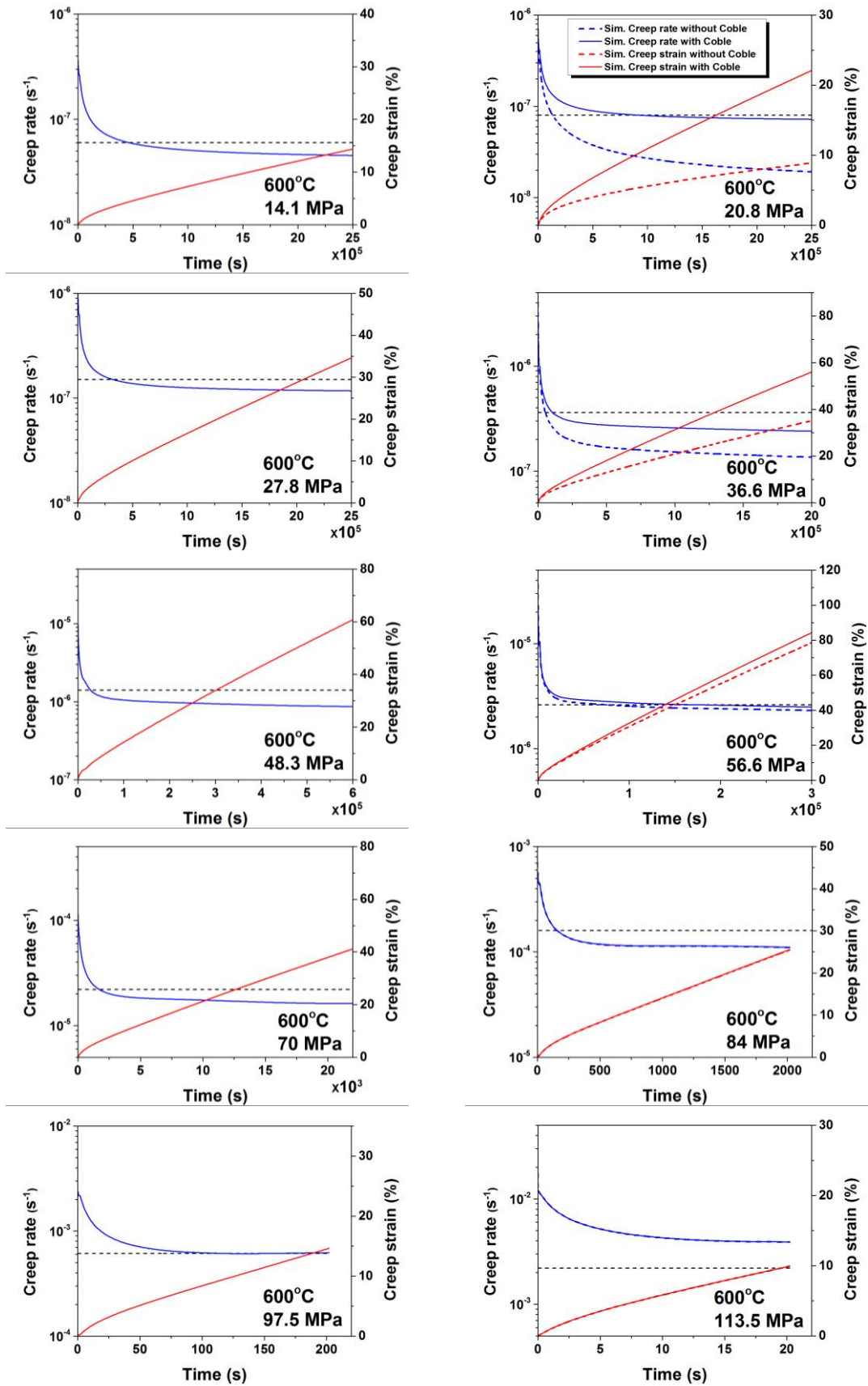


Fig. 10. Predicted creep rate and creep strain for Zircaloy-4 at 600°C for various stresses. Horizontal dash lines represent the measured steady-state creep rate in Kombaiah and Murty (2015a, 2015b).

## 5 Discussion

Although the core-diffusion theory is capable of capturing the transition between moderate and high-stress regimes via  $\Delta\tau_m^s(t_{a,loca}^s)$ , an alternative hypothesis can be posed related to the solute dragging mechanism. A dislocation traveling freely within the matrix will interact with the solutes around it and will experience a dragging stress as resistance to glide. The solute dragging stress has been studied by atomistic simulations, i.e. (Sills and Cai, 2015; Yoshinaga and Morozumi, 1971). It has been demonstrated that it increases almost linearly with the dislocation velocity, then reaches a maximum value after a short transient process, and starts to decrease afterward. The stresses acting on a moving dislocation include the applied resolved shear stress, lattice friction, solute dragging stress ( $\tau_{sd}$ ) and the contribution from phonon dragging ( $\tau_{pd}$ ). At quasi-static state, the dislocation can travel at a constant speed since the stresses are in balance as  $\tau^s - \tau_0^s = \tau_{sd} + \tau_{pd}$ . The solute-dragged dislocations move at low velocity (of order 10 nm/s according to Caillard, 2015), which leads to a higher travel time mentioned in Eq. 7 and thus lower creep rate. At such speed, the phonon drag stress is negligible since the phonon damping coefficient is very low. However, if  $\tau^s - \tau_0^s$  exceeds the maximum solute dragging stress, the dislocation can accelerate until the balance is restored by the phonon drag stress. Resulting from the extreme low phonon damping coefficient (of order 1 MPa·s/m), the dislocations need to reach around 1m/s velocity even if only 1 MPa of phonon drag stress is required. This ‘jump’ occurs at the sub-material point level. As a consequence, the creep rate in one material point and in the polycrystal may experience a fast increase at high-stress regime. However, it has been reported that a dislocation pinned for a long period of time will accumulate high pinning stresses. When unpinned, it will immediately achieve a very high velocity, until it is immobilized again by the next obstacle (Castany et al., 2007). Since this introduces some uncertainties in the effect of solute dragging on the dislocation motion, solute dragging is not accounted for explicitly in this work. Its effects are accounted for in the waiting time term, which may, in turn, introduce errors in the parameter calibrations.

The  $\Delta\tau_l^s$  term in Eq. 22 describes the junction strength change due to the core-diffusion of solutes. According to Soare and Curtin (2008a), this term is responsible for capturing the dip of SRS appearing at certain temperature intervals. The anomalous SRS in Zr alloys is analyzed in several works, i.e. (Graff, 2006; Lee et al., 2001). In Lee et al. (2001), the SRS of Zircaloy-4 is measured for strain rates of  $1.33 \cdot 10^{-4} \text{ s}^{-1}$ ,  $6.67 \cdot 10^{-4} \text{ s}^{-1}$  and  $3.33 \cdot 10^{-3} \text{ s}^{-1}$  at various temperatures, and the SRS anomaly appears around 600-700K depending on the strain rate. Although the experimental data are limited to a few strain rates, one may observe that the dips in SRS appear at higher temperature for higher strain rates.

Following the definition of SRS in Lee et al. (2001), the SRS in this work is determined as follows: monotonic tensile tests are performed at strain rates of  $\&$

(target strain rate with values taken after Lee et al.) and  $\dot{\epsilon}_2 = 0.9\dot{\epsilon}_1$ . When the tests reach certain strain level  $\epsilon_{SRS}$ , the flow stresses are recorded, and denoted as  $\sigma_1$  and  $\sigma_2$ , respectively. Such tests are repeated for various temperatures, and the SRS for each temperature is calculated as:

$$SRS = \frac{\ln \sigma_1 - \ln \sigma_2}{\ln \dot{\epsilon}_1 - \ln \dot{\epsilon}_2} \quad (30)$$

As mentioned in section 2, the effective dislocation-dislocation junction strength  $\Delta\tau_i^s$  is a function of the aging time of the dislocations acting as obstacles. The principle for the anomalous SRS is that for lower strain rate the dislocation obstacles have more time to age before  $\epsilon_{SRS}$  is achieved, which results in a higher junction strength and thus higher critical stress required to unpin. Therefore, a low SRS tends to appear when the aging time is approaching the reference diffusion time  $t_d$ . According to Eqs. 20-22, the junction strength change is controlled by the aging time and the aging strength factor  $\delta = \chi\Delta E_\infty^{core}/A$ . Using the parameters given in section 3, the SRSs for Zircaloy-4 are predicted with  $\chi=20, 100$  and  $500$  at  $\epsilon_{SRS} = 3\%$ , and the results for the three strain rates are plotted in Figs. 11a-c. It can be seen that the dips in the SRS are found for all strain rates but only with  $\chi = 500$ . For the most active prismatic slip, at 573K the aging strength factor is  $\delta \approx 0.132, 0.66$  and  $3.31$  for  $\chi = 20, 100$  and  $500$ , respectively. For reference, using the parameters given in Soare and Curtin (2008a), the factor  $\delta$  at the same temperature for Al-5%Mg is about 0.322. The reason for the required high  $\delta$  value is that the dislocation density in Zircaloy-4 is very low. The predicted line tension in the absence of solutes is around 5.3MPa (prismatic slip) using the initial dislocation density given in section 3. Hence, for  $\chi=20, 100$  and  $500$  the line tension resistance changes due to the core-diffusion is 0.7MPa, 3.5MPa and 17.5MPa, respectively. As presented in Fig. 11d, only at  $\chi=500$  the  $\Delta\tau_i^s$  term is strong enough to affect evidently the flow stresses at 3% strain. In Fig. 12, the predicted SRSs using  $\chi=500$  are compared with the experimental data. It shows that generally the model is able to capture the magnitude of SRS and the temperatures where the dips are presented. The results in Figs. 11 and 12 indicate that  $\Delta\tau_i^s$  affects the SRS in the way expected but it requires very high contribution of the solute core-diffusion on the junction strength to achieve an evident dip in SRS.

The high value of the parameter  $\chi=500$  compared to  $\chi=8.7$  reported by Soare and Curtin (2008a) or  $\chi=20$  derived in the previous sections may be attributed to several factors. First, in Soare and Curtin (2008a), the value  $\chi=8.7$  is determined based on the linear relationship between  $\Delta E^{core}$  and  $\Delta\tau_i^s$  obtained from mesoscopic simulation of diffusion of substitutional Mg solutes around edge dislocations in FCC Al-Mg system. For HCP Zr alloy, the dislocation core structure and the dislocation-dislocation junctions are obviously different, and the effect of

core-diffusion mechanism on screw dislocations is unknown. The presence of interstitial solutes (Oxygen) may also affect the aging process and the resulting dislocation behavior. In addition, as discussed above, the low dislocation density used in the simulation is partly responsible for the high  $\chi$  required to achieve the experimental SRS reported by Lee et al. (2001). Notice that the parameters used in this work aim to capture the mechanical behaviors of recrystallized Zircaloy-4 (Kombaiah and Murty, 2015a, 2015b) whereas Lee et al. performed the tests on cold-worked Zircaloy-4 tubes. Since the cold-worked material usually has a higher dislocation density, the  $\chi$  parameter may be overestimated. However, the dislocation density of the material is not reported in Lee et al.(2001). Therefore, while we have proven in this work that the general mathematical form of this model is capable of capturing the anomalous SRS, the prediction of the mechanical response for cold-worked Zircaloy-4 is outside the scope of the current work. Moreover, the dislocation density may also affect the available number of solutes for each unit length of dislocation segment. Without considering such factor, the local binding energy may be over or underestimated, and thus affect the calibration of the parameter  $\chi$ . Elucidating the core-diffusion process in Zr alloy and deriving the relevant ( $\chi$ ,  $\Delta E_{\infty}^{core}$ ) parameters would require further atomistic analysis.

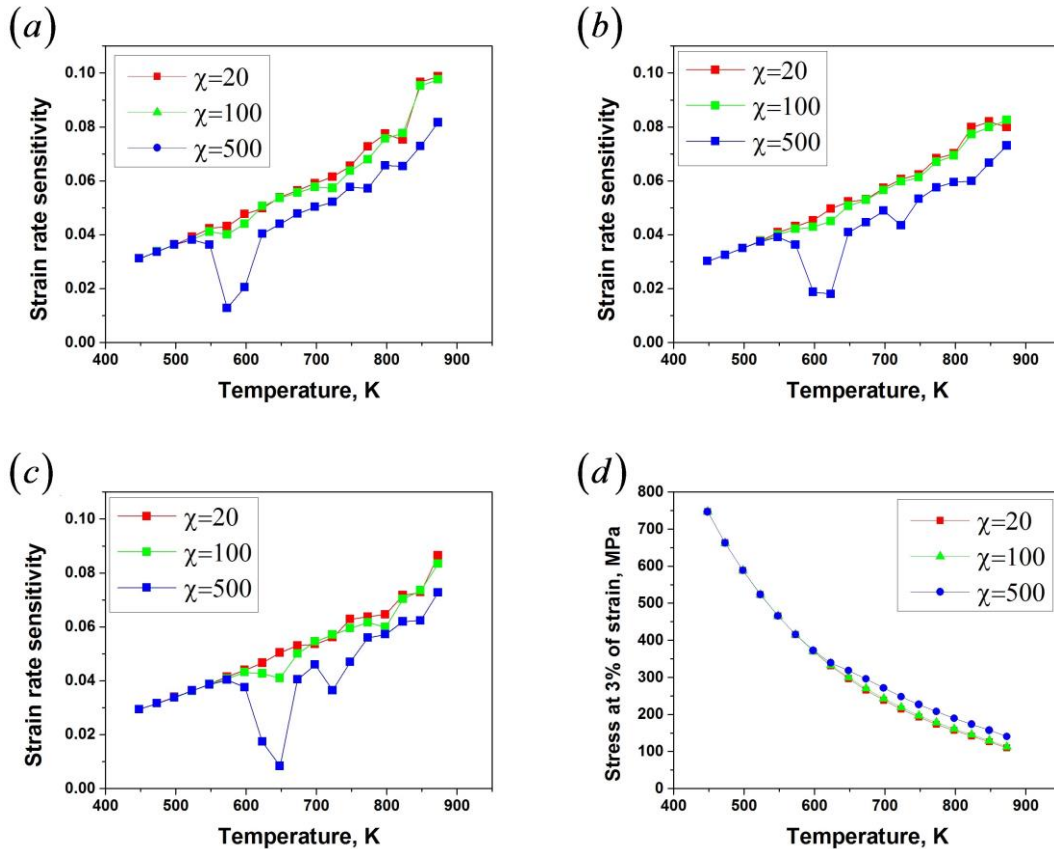


Fig. 11. Predicted SRS at strain rates of (a)  $1.33 \cdot 10^{-4} \text{ s}^{-1}$ , (b)  $6.67 \cdot 10^{-4} \text{ s}^{-1}$  and (c)  $3.33 \cdot 10^{-3} \text{ s}^{-1}$ . (d) Predicted flow stress at 3% strain for strain rate of  $3.33 \cdot 10^{-3} \text{ s}^{-1}$ .

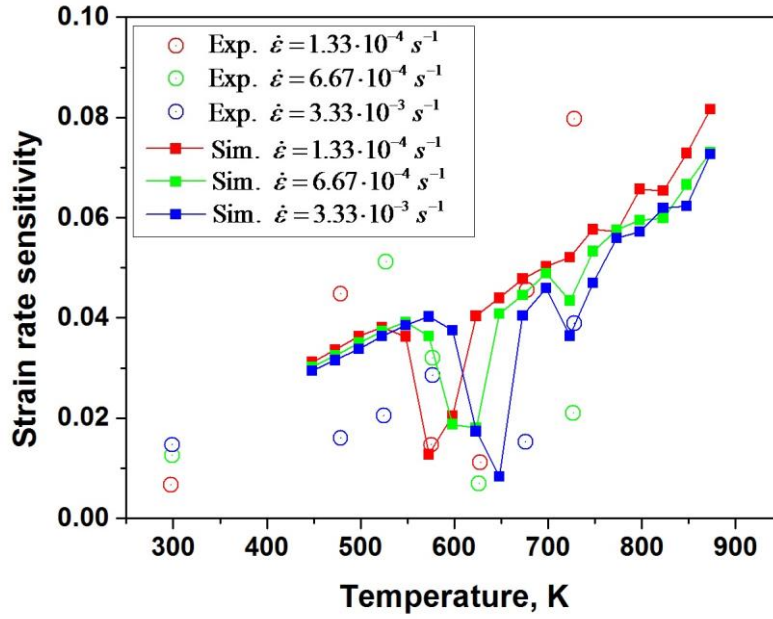


Fig. 12. Predicted SRS using  $\chi = 500$  as function of temperature. Experimental data from Lee et al. (2001).

In the present work, the dislocation climb mechanism is not included in the simulation because we assume that climb is inhibited by the presence of solutes. When an edge dislocation is clustered, the surrounding impurities tend to affect the stress field around the dislocation, which leads to an increase in the required driving stress for climb. Moreover, the solutes may also disturb the diffusion of point defects into the edge dislocations. In addition, the in-situ TEM study performed by Caillard et al. (2015) proved that the dislocation jogs, which are edge in character, never climb, even though they are under an extra driving force (besides the climb component of Peach-Koehler force): the line tension from the jogged screw segments.

## 6 Conclusions and Perspectives

In this work, a crystallographic thermal creep model is proposed for Zr alloys considering the hardening contribution of solutes. The core-diffusion model proposed by Soare and Curtin (2008a) is coupled with the transition state theory framework (Wang et al., 2016, 2017) accounting for the heterogeneously distributed internal stresses within material points. The simulation results show that this model, which is embedded in the crystallographic VPSC framework, is capable to reproduce the experimental creep data for Zircaloy-4, especially the transition between the power law creep regimes and the anomalous strain rate sensitivity. This is achieved through the dependence of the binding energy on waiting time through the core-diffusion of solutes.

The increase in binding energy should also affect the junction strength, which is responsible for the anomalous strain rate sensitivity. Our analysis shows that a very

high contribution of the core-diffusion to the junction strength is required to substantially influence the SRS in Zircaloy-4. More experimental and atomistic-level simulation studies are necessary to verify this specific result in the future.

Keeping in mind the challenges associated with performing creep experiments in general, and with determining steady state conditions in particular, the mechanism-based model reasonably captures results from a panoply of tests covering the 500-600°C interval, and stresses spanning 14 to 156 MPa. The corresponding experimental and predicted steady state creep rates vary between  $1.5 \cdot 10^{-9} \text{s}^{-1}$  to  $2 \cdot 10^{-3} \text{s}^{-1}$ , which represents an interval of about 6 orders of magnitude. Note that there may be uncertainties in the determination of steady-state stage in experiments, which will affect the accuracy of the data. The creep rate evolution curves, presenting both the primary and steady-state stages, are more reliable for the validation of this model.

## **Acknowledgement**

This work was supported by the Consortium for Advanced Simulation of Light Water Reactor (CASL), an Energy Innovation Hub under US Department of Energy Contract No. DE-AC05-00OR22725. The authors would like to acknowledge the detailed evaluation and insightful comments from one of the reviewers that allowed us to introduce corrections in the model and to improve the conceptual content of the related discussions.

## References:

- Akhtar, A., 1975. Prismatic slip in zirconium single crystals at elevated temperatures. *Metall. Trans. A* 6, 1217–1222. doi:10.1007/BF02658531
- Akhtar, A., 1973a. Compression of zirconium single crystals parallel to the c-axis. *J. Nucl. Mater.* 47, 79–86. doi:10.1016/0022-3115(73)90189-X
- Akhtar, A., 1973b. Basal slip in zirconium. *Acta Metall.* 21, 1–11. doi:10.1016/0001-6160(73)90213-7
- Akhtar, A., Teghtsoonian, A., 1971. Plastic deformation of zirconium single crystals. *Acta Metall.* 19, 655–663. doi:10.1016/0001-6160(71)90019-8
- Austin, R.A., McDowell, D.L., 2011. A dislocation-based constitutive model for viscoplastic deformation of fcc metals at very high strain rates. *Int. J. Plast.* 27, 1–24. doi:10.1016/j.ijplas.2010.03.002
- Barrett, C., Nix, W., 1965. A model for steady state creep based on the motion of jogged screw dislocations. *Acta Metall.* 13, 1247–1258. doi:10.1016/0001-6160(65)90034-9
- Basirat, M., Shrestha, T., Potirniche, G.P., Charit, I., Rink, K., 2012. A study of the creep behavior of modified 9Cr-1Mo steel using continuum-damage modeling. *Int. J. Plast.* 37, 95–107. doi:10.1016/j.ijplas.2012.04.004
- Bertin, N., Tomé, C.N., Beyerlein, I.J., Barnett, M.R., Capolungo, L., 2014. On the strength of dislocation interactions and their effect on latent hardening in pure Magnesium. *Int. J. Plast.* 62, 72–92. doi:10.1016/j.ijplas.2014.06.010
- Beyerlein, I.J., Tomé, C.N., 2008. A dislocation-based constitutive law for pure Zr including temperature effects. *Int. J. Plast.* 24, 867–895. doi:10.1016/j.ijplas.2007.07.017
- Caillard, D., Rautenberg, M., Feaugas, X., 2015. Dislocation mechanisms in a zirconium alloy in the high-temperature regime: An in situ TEM investigation. *Acta Mater.* 87, 283–292. doi:10.1016/j.actamat.2015.01.016
- Castany, P., Pettinari-Sturmel, F., Crestou, J., Douin, J., Coujou, A., 2007. Experimental study of dislocation mobility in a Ti-6Al-4V alloy. *Acta Mater.* 55, 6284–6291. doi:10.1016/j.actamat.2007.07.032
- Charit, I., Murty, K.L., 2008. Creep behavior of niobium-modified zirconium alloys. *J. Nucl. Mater.* 374, 354–363. doi:10.1016/j.jnucmat.2007.08.019
- Coble, R.L., 1963. A model for boundary diffusion controlled creep in polycrystalline materials. *J. Appl. Phys.* 34, 1679–1684.

- Cottrell, A.H., 1948. Effect of solute atoms on the behaviour of dislocations. Rep. a Conf. Strength Solids, Phys. Soc. London.
- Cottrell, A.H., Jaswon, M.A., 1949. Distribution of solute atoms round a slow dislocation. Proc. R. Soc. Lond. A. Math. Phys. Sci. doi:10.1098/rspa.1983.0054
- Curtin, W.A., Olmsted, D.L., Hector, L.G., 2006. A predictive mechanism for dynamic strain ageing in aluminium–magnesium alloys. Nat. Mater. 5, 875–880. doi:10.1038/nmat1765
- Ecob, R.C., Donaldson, A.T., 1985. A microstructural investigation of steady state creep of zircaloy-4 at 973 K. J. Nucl. Mater. 132, 110–125. doi:10.1016/0022-3115(85)90405-2
- Estrin, Y., 1998. Dislocation theory based constitutive modelling: foundations and applications. J. Mater. Process. Technol. 80–81, 33–39. doi:10.1016/s0924-0136(98)00208-8
- Fleischer, R.L., 1966. Substitutional solution hardening of copper. Acta Metall. 14, 1867–1868. doi:10.1016/0001-6160(66)90045-9
- Franciosi, P., Zaoui, A., 1982. Multislip in f.c.c. crystals a theoretical approach compared with experimental data. Acta Metall. 30, 1627–1637. doi:10.1016/0001-6160(82)90184-5
- Gaffard, V., Gourgues-Lorenzon, A.F., Besson, J., 2005. High temperature creep flow and damage properties of 9Cr1MoNbV steels: Base metal and weldment. Nucl. Eng. Des. 235, 2547–2562. doi:10.1016/j.nucengdes.2005.07.001
- Garber, R.I., Gindin, I.A., Yu, U., Shubin, V., 1963. Slipping of beryllium single crystals along the hexagonal axis in the temperature range, 4.2–900 K. Sov. Phys. Solid State 5, 315–320.
- Garde, A.M., Chung, H.M., Kassner, T.F., 1978. Micrograin superplasticity in Zircaloy at 850°C. Acta Metall. 26, 153–166. doi:10.1016/0001-6160(78)90212-2
- Graff, S., 2006. Viscoplastic behavior of zirconium alloys in the temperatures range 20°C–400°C : characterization and modeling of strain ageing phenomena. Ph.D thesis.
- Granato, A. V., Lücker, K., Schlipf, J., Teutonico, L.J., 1964. Entropy Factors for Thermally Activated Unpinning of Dislocations. J. Appl. Phys. 35, 2732. doi:10.1063/1.1713833
- Groma, I., Bakó, B., 1998. Probability distribution of internal stresses in parallel straight dislocation systems. Phys. Rev. B 58, 2969–2974.

doi:10.1103/PhysRevB.58.2969

- Groma, I., Székely, F., 2000. Analysis of the asymptotic properties of X-ray line broadening caused by dislocations. *J. Appl. Crystallogr.* 33, 1329–1334. doi:10.1107/S002188980001058X
- Hayes, T. a., Kassner, M.E., Rosen, R.S., 2002. Steady-state creep of  $\alpha$ -zirconium at temperatures up to 850 °C. *Metall. Mater. Trans. A* 33, 337–343. doi:10.1007/s11661-002-0095-4
- Hirth, J.P., Lothe, J., 1983. *Theory of Dislocations* (2nd ed.). *J. Appl. Mech.* 50, 476. doi:10.1115/1.3167075
- J. Friedel, 1956. *Les dislocations*. Gauthier-Villars Paris.
- Kalácska, S., Groma, I., Borbély, A., Ispánovity, P.D., 2017. Comparison of the dislocation density obtained by HR-EBSD and X-ray profile analysis. *Appl. Phys. Lett.* 110. doi:10.1063/1.4977569
- Kanitpanyacharoen, W., Merkel, S., Miyagi, L., Kaercher, P., Tomé, C.N., Wang, Y., Wenk, H.R., 2012. Significance of mechanical twinning in hexagonal metals at high pressure. *Acta Mater.* 60, 430–442. doi:10.1016/j.actamat.2011.07.055
- Kitayama, K., Tomé, C.N., Rauch, E.F., Gracio, J.J., Barlat, F., 2013. A crystallographic dislocation model for describing hardening of polycrystals during strain path changes. Application to low carbon steels. *Int. J. Plast.* 46, 54–69. doi:10.1016/j.ijplas.2012.09.004
- Kocks, U.F., Argon, A.S., Ashby, M.F., 1975. Thermodynamics and Kinetics of Slip. *Prog. Mater. Sci.* 19, 171–229. doi:10.1016/0079-6425(75)90009-2
- Kocks, U.F., Mecking, H., 2003. Physics and phenomenology of strain hardening: The FCC case. *Prog. Mater. Sci.* doi:10.1016/S0079-6425(02)00003-8
- Kombaiah, B., Murty, K.L., 2015a. Dislocation cross-slip controlled creep in Zircaloy-4 at high stresses. *Mater. Sci. Eng. A* 623, 114–123. doi:10.1016/j.msea.2014.11.040
- Kombaiah, B., Murty, K.L., 2015b. High temperature creep and deformation microstructures in recrystallized Zircaloy-4. *Philos. Mag.* 95, 1656–1679. doi:10.1080/14786435.2015.1042939
- Labusch, R., 1970. A Statistical Theory of Solid Solution Hardening. *Phys. Status Solidi* 41, 659–669. doi:10.1002/pssb.19700410221
- Lebensohn, R.A., Tomé, C.N., 1993. A self-consistent anisotropic approach for the simulation of plastic deformation and texture development of polycrystals:

- Application to zirconium alloys. *Acta Metall. Mater.* 41, 2611–2624.  
doi:10.1016/0956-7151(93)90130-K
- Lebensohn, R.A., Tomé, C.N., Castañeda, P.P., 2007. Self-consistent modelling of the mechanical behaviour of viscoplastic polycrystals incorporating intragranular field fluctuations. *Philos. Mag.* 87, 4287–4322.  
doi:10.1080/14786430701432619
- Lee, K.W., Kim, S.K., Kim, K.T., Hong, S.I., 2001. Ductility and strain rate sensitivity of Zircaloy-4 nuclear fuel claddings. *J. Nucl. Mater.* 295, 21–26.  
doi:10.1016/S0022-3115(01)00509-8
- Leyson, G.P.M., Curtin, W.A., 2016. Solute strengthening at high temperatures. *Model. Simul. Mater. Sci. Eng.* 24, 65005. doi:10.1088/0965-0393/24/6/065005
- Leyson, G.P.M., Curtin, W.A., 2013. Friedel vs. Labusch: the strong/weak pinning transition in solute strengthened metals. *Philos. Mag.* 93, 2428–2444.  
doi:10.1080/14786435.2013.776718
- Lloyd, J.T., Clayton, J.D., Austin, R.A., McDowell, D.L., 2014. Plane wave simulation of elastic-viscoplastic single crystals. *J. Mech. Phys. Solids* 69, 14–32.  
doi:10.1016/j.jmps.2014.04.009
- Masson, R., Bornert, M., Suquet, P., Zaoui, A., 2000. Affine formulation for the prediction of the effective properties of nonlinear composites and polycrystals. *J. Mech. Phys. Solids* 48, 1203–1227. doi:10.1016/S0022-5096(99)00071-X
- Mecking, H., Kocks, U.F., 1981. Kinetics of flow and strain-hardening. *Acta Metall.* 29, 1865–1875. doi:10.1016/0001-6160(81)90112-7
- Moon, J.H., Cantonwine, P.E., Anderson, K.R., Karthikeyan, S., Mills, M.J., 2006. Characterization and modeling of creep mechanisms in Zircaloy-4. *J. Nucl. Mater.* 353, 177–189. doi:10.1016/j.jnucmat.2006.01.023
- Morrow, B.M., Kozar, R.W., Anderson, K.R., Mills, M.J., 2016. Substructure evolution of Zircaloy-4 during creep and implications for the Modified Jogged-Screw model. *Mater. Sci. Eng. A* 665, 90–97.  
doi:10.1016/j.msea.2016.04.016
- Morrow, B.M., Kozar, R.W., Anderson, K.R., Mills, M.J., 2013. An examination of the use of the Modified Jogged-Screw model for predicting creep behavior in Zircaloy-4. *Acta Mater.* 61, 4452–4460. doi:10.1016/j.actamat.2013.04.014
- Murty, K.L., Dentel, G., Britt, J., 2005. Effect of temperature on transitions in creep mechanisms in class-A alloys. *Mater. Sci. Eng. A* 410–411, 28–31.  
doi:10.1016/j.msea.2005.08.006

- Nes, E., 1997. Modelling of work hardening and stress saturation in FCC metals. *Prog. Mater. Sci.* 41, 129–193. doi:10.1016/S0079-6425(97)00032-7
- Olmsted, D.L., Hector, L.G., Curtin, W.A., 2006. Molecular dynamics study of solute strengthening in Al/Mg alloys. *J. Mech. Phys. Solids* 54, 1763–1788. doi:10.1016/j.jmps.2005.12.008
- Onimus, F., Béchade, J.L., Gilbon, D., 2013. Experimental analysis of slip systems activation in neutron-irradiated zirconium alloys and comparison with polycrystalline model simulations. *Metall. Mater. Trans. A Phys. Metall. Mater. Sci.* 44, 45–60. doi:10.1007/s11661-012-1463-3
- Pahutová, M., Čadek, J., Černý, V., 1976. Steady state creep of ZrNb alloys in a temperature interval 350 to 550°C. *J. Nucl. Mater.* 61, 285–296. doi:10.1016/0022-3115(76)90267-1
- Picu, R.C., 2004. A mechanism for the negative strain-rate sensitivity of dilute solid solutions. *Acta Mater.* 52, 3447–3458. doi:10.1016/j.actamat.2004.03.042
- Poirier, J.P., 1976. On the symmetrical role of cross-slip of screw dislocations and climb of edge dislocations as recovery processes controlling high-temperature creep. *Rev. Phys. Appliquée* 11, 731–738. doi:10.1051/rphysap:01976001106073100
- Rosinger, H.E., Bera, P.C., Clendening, W.R., 1979. Steady-state creep of zircaloy-4 fuel cladding from 940 to 1873 K. *J. Nucl. Mater.* 82, 286–297. doi:10.1016/0022-3115(79)90011-4
- Sills, R.B., Cai, W., 2015. Solute Drag on Perfect and Extended Dislocations. *Philos. Mag.* 0, 1–27. doi:10.1080/14786435.2016.1142677
- Soare, M.A., Curtin, W.A., 2008a. Solute strengthening of both mobile and forest dislocations: The origin of dynamic strain aging in fcc metals. *Acta Mater.* 56, 4046–4061. doi:10.1016/j.actamat.2008.04.027
- Soare, M.A., Curtin, W.A., 2008b. Single-mechanism rate theory for dynamic strain aging in fcc metals. *Acta Mater.* 56, 4091–4101. doi:10.1016/j.actamat.2008.04.030
- Viswanathan, G.B., Karthikeyan, S., Mills, M.J., Hayes, R.W., 2002. Application of a modified jogged-screw model for creep of TiAl and  $\alpha$ -Ti alloys. *Metall. Mater. Trans. A* 33, 329–336. doi:10.1007/s11661-002-0094-5
- Viswanathan, G.B., Vasudevan, V.K., Mills, M.J., 1999. Modification of the jogged-screw model for creep of  $\gamma$ -TiAl. *Acta Mater.* 47, 1399–1411. doi:10.1016/S1359-6454(99)00021-X

- Wang, H., Capolungo, L., Clausen, B., Tomé, C.N., 2017. A crystal plasticity model based on transition state theory. *Int. J. Plast.* 93, 251–268. doi:10.1016/j.ijplas.2016.05.003
- Wang, H., Clausen, B., Capolungo, L., Beyerlein, I.J., Wang, J., Tomé, C.N., 2016. Stress and strain relaxation in magnesium AZ31 rolled plate: In-situ neutron measurement and elastic viscoplastic polycrystal modeling. *Int. J. Plast.* 79, 275–292. doi:10.1016/j.ijplas.2015.07.004
- Wang, H., Wu, P.D., Tomé, C.N., Huang, Y., 2010. A finite strain elastic-viscoplastic self-consistent model for polycrystalline materials. *J. Mech. Phys. Solids* 58, 594–612. doi:10.1016/j.jmps.2010.01.004
- Warda, R.D., Fidleris, V., Teghtsoonian, E., 1973. Dynamic Strain Aging During Creep of  $\alpha$ -Zr 4.
- Wen, W., Borodachenkova, M., Tomé, C.N., Vincze, G., Rauch, E.F., Barlat, F., Grácio, J.J., 2016. Mechanical behavior of low carbon steel subjected to strain path changes: Experiments and modeling. *Acta Mater.* 111, 305–314. doi:10.1016/j.actamat.2016.03.075
- Wen, W., Borodachenkova, M., Tomé, C.N., Vincze, G., Rauch, E.F., Barlat, F., Grácio, J.J., 2015. Mechanical behavior of Mg subjected to strain path changes: Experiments and modeling. *Int. J. Plast.* 73, 171–183. doi:10.1016/j.ijplas.2014.10.009
- Wilkins, M., 1970. The determination of density and distribution of dislocations in deformed single crystals from broadened X - ray diffraction profiles. *Phys. Status Solidi* 2, 359–370. doi:10.1002/pssa.19700020224
- Wilkinson, A.J., Tarleton, E., Vilalta-clemente, A., Jiang, J., Britton, T.B., David, M., Wilkinson, A.J., Tarleton, E., Vilalta-clemente, A., Jiang, J., Britton, T.B., Collins, D.M., 2014. Measurement of probability distributions for internal stresses in dislocated crystals Measurement of probability distributions for internal stresses in dislocated crystals 181907, 0–5. doi:10.1063/1.4901219
- Yoshinaga, H., Morozumi, S., 1971. The solute atmosphere round a moving dislocation and its dragging stress. *Philos. Mag.* 23, 1367–1385. doi:10.1080/14786437108217008
- Zaiser, M., 2002. Dislocation motion in a random solid solution. *Philos. Mag. A* 82, 2869–2883. doi:10.1080/01418610210157968
- Zhang, F., Curtin, W.A., 2008. Atomistically informed solute drag in Al–Mg. *Model. Simul. Mater. Sci. Eng.* 16, 55006. doi:10.1088/0965-0393/16/5/055006



## FIGURE CAPTIONS

Fig. 1. Experimental steady-state creep rate reported in Kombaiah and Murty (2015a, 2015b).

Fig. 2. Initial texture of rolled Zr alloy. RD and TD represent rolling and transverse directions, respectively.

Fig. 3. Dependence of lattice friction with temperature in pure Zr for: (a) prismatic slip, experimental data from Akhtar (Akhtar, 1975) and Akhtar and Teghtsoonian (Akhtar and Teghtsoonian, 1971); (b) basal slip, experimental data from Akhtar (Akhtar, 1973b); (c) pyramidal<c+a> slip, experimental data from Akhtar (Akhtar, 1973a) and Garber et al (Garber et al., 1963)

Fig. 4.  $\tau_s$  values used in the simulations obtained using Eq. 37.

Fig. 5. Predicted initial creep rates at 500, 550 and 600°C demonstrating the role of the local aging time-dependent term  $\Delta\tau_m^s$ . Results from the core-diffusion model with

$\Delta\tau_m^s(t_{a,local}^s)$  (solid lines) are compared with using  $\Delta\tau_m^s = 0$  (upper dash lines) and

$\Delta\tau_m^s = \Delta\tau_{m,\infty}^s$  (lower dash lines)

Fig. 6. Comparison between predictions and experimental data. Triangles represent the experimental steady-state creep rates in Kombaiah and Murty (2015a, 2015b); circles represent the predicted saturation creep rates.

Fig. 7. Predicted creep rate and creep strain for Zircaloy-4 for 129MPa (500°C) and 60.6MPa (550°C). Experimental data from Kombaiah and Murty (2015a, 2015b).

Fig. 8. Predicted creep rate and creep strain for Zircaloy-4 at 500°C for various stresses. Horizontal dash lines represent the measured steady-state creep rate in Kombaiah and Murty (2015a, 2015b).

Fig. 9. Predicted creep rate and creep strain for Zircaloy-4 at 550°C for various stresses. Horizontal dash lines represent the measured steady-state creep rate in Kombaiah and Murty (2015a, 2015b).

Fig. 10. Predicted creep rate and creep strain for Zircaloy-4 at 600°C for various stresses. Horizontal dash lines represent the measured steady-state creep rate in Kombaiah and Murty (2015a, 2015b).

Fig. 11. Predicted SRS at strain rates of (a)  $1.33 \cdot 10^{-4} \text{ s}^{-1}$ , (b)  $6.67 \cdot 10^{-4} \text{ s}^{-1}$  and (c)  $3.33 \cdot 10^{-3} \text{ s}^{-1}$ ; Predicted flow stress at 3% of strain for strain rate of  $3.33 \cdot 10^{-3} \text{ s}^{-1}$  (d).

Fig. 12. Predicted SRS using  $\chi = 500$  as function of temperature. Experimental data from Lee et al. (2001).

Tab. 1. Parameters used for the Zircaloy-4 in this work

Tab. 2. Core-diffusion related parameters for Zircaloy-4